

1 **Rift propagation in rotational versus orthogonal extension: insights from 4D**  
2 **analogue models**

3  
4 **Creative Commons licence: CC BY-NC-ND 4.0**

5 **Link to final publication in Journal of Structural Geology (Elsevier):**

6 <https://doi.org/10.1016/j.jsg.2019.103946>

7  
8  
9 Frank Zwaan<sup>a\*</sup>, Guido Schreurs<sup>a</sup>, Matthias Rosenau<sup>b</sup>

10  
11 a) Institute of Geological Sciences, University of Bern, Baltzerstrasse 1+3, CH-3012 Bern,  
12 Switzerland

13 b) Helmholtz Centre Potsdam German Research Centre for Geosciences GFZ,  
14 Telegrafenberg, Potsdam 14473, Germany

15  
16 \*frank.zwaan@geo.unibe.ch, fzwaan@hotmail.com (F. Zwaan) Tel: +31634081562

17  
18 **ORCID:**

19  
20 Frank Zwaan <https://orcid.org/0000-0001-8226-2132>

21 Guido Schreurs <https://orcid.org/0000-0002-4544-7514>

22 Matthias Rosenau <http://orcid.org/0000-0003-1134-5381>

23  
24  
25 **Keywords:** Rotational extension, analogue modeling, structural gradients, rifting, rift  
26 propagation, boundary effects, scissor tectonics

27  
28  
29  
30 **Abstract**

31  
32 In rift settings, extension rates often vary along strike, due to rotation about a vertical axis or  
33 Euler pole, yet tectonic modelers traditionally apply constant along-strike deformation rates.  
34 Here we compare rift development and propagation under traditional orthogonal extension  
35 versus rotational extension conditions.

36  
37 The set-ups involve brittle-viscous layering and localize deformation through structural  
38 weaknesses (seeds). Our models provide first-order insights into the differences in rift  
39 development between both boundary conditions: orthogonal extension produces a rift basin  
40 with constant synchronous along-strike features, whereas rotational extension induces  
41 along-strike structural gradients, diachronous rift development causing rift propagation and  
42 the development of V-shaped basins. We observe important viscous flow associated with  
43 differential pressure gradients in rotational extension. We also describe the important  
44 effects of strain partitioning between rift axis and model boundaries, the quantifying of  
45 which is crucial to avoid incorrect model interpretations.

46  
47 Although our model results are first-order only, they are in good agreement with various  
48 natural examples and previous modeling studies and highlight the importance of  
49 considering the third dimension when studying tectonic systems.

50

## 51 1. Introduction

52  
53 The evolution and propagation of rift basins is an important topic in extensional tectonics.  
54 Traditionally, rift systems were assumed to develop under constant along-strike extension  
55 conditions (i.e. constant strain, e.g. Vink 1980, Fig. 1a). Rifts then nucleate along  
56 lithospheric weaknesses, for instance produced by mantle plumes, and propagate away  
57 from these into stronger parts of the lithosphere where extension was previously  
58 accommodated by distributed deformation (e.g. Courtillot 1982; Hey et al. 2010). When  
59 extension persists, such propagating rift basins would develop into large-scale rift systems,  
60 which may ultimately lead to continental break-up.

61  
62 In many rift settings however, extension rates vary along strike, due to pivoting motion  
63 about a rotation axis for small-scale (regional) settings or about an Euler pole for global-  
64 scale systems (Figs. 1b, c, 2). These extension gradients are associated with the  
65 propagation of rift structures or whole oceanic basins, exemplified by the formation of  
66 characteristic “V-shaped basins” (e.g. Martin 1984; Péron-Pinvidic & Manatschal 2010;  
67 Fletcher et al. 2013; Fig. 1b, c). Examples are found in the Gulf of Aden and Red Sea  
68 region, due to the counter clockwise rotation of the Arabian plate (Bellahsen et al. 2003;  
69 ArRajehi et al. 2010; Fig. 2a) and along the NE Atlantic continental margin, with various V-  
70 shaped basins having formed during continental break-up (Péron-Pinvidic & Manatschal  
71 2010, Fig. 2d). Also along the Gakkel Ridge in the Arctic extension rates decrease towards  
72 Siberia (Dick et al. 2003; DeMets et al. 2010, Fig 2f). The associated plate boundary enters  
73 the Eurasian continent at the Laptev Margin, where extension becomes diffuse (e.g. Van  
74 Wijk & Blackman 2005; Franke & Hinz 2009, Fig. 2f).

75  
76 Similar settings involving an oceanic spreading center entering a continental domain are  
77 found in the Havre Trough/Taupo Rift system in New Zealand (Benes & Scott 1996, Fig. 2h)  
78 and the Woodlark Basin off Papua New Guinea (Benes et al. 1994; Taylor et al. 1999, Fig.  
79 2g). In the case of the Laptev Margin, the plate boundary continues into Siberia and enters  
80 a compressive regime at the Chersky Range on the opposite side of the Euler pole  
81 (Glebovsky et al. 2006; Fujita et al. 2009; Imaeva et al. 2016, Fig. 2f). Note that while such  
82 rotational extension has been referred to as “scissor extension” (e.g. Zhou et al. 1995; Le  
83 Pourhiet et al. 2018), this term is actually not appropriate as it implies extension on both  
84 sides of the pivot point (Fig. 1d). For the settings studied here, which follow more the  
85 motions of a laundry peg (Fig. 1d), we therefore prefer to use the term “rotational tectonics”.  
86 Rotation-type transitions from extension to contraction may also develop in back-arc  
87 systems due to rotational motion between the down-going and overriding plate (Seebeck et  
88 al. 2014), for instance in the above-mentioned Taupo Rift/Havre Trough system and  
89 possibly in the Woodlark Basin (Fig. 2g, h), and various other basins around the globe as  
90 well (Wallace et al. 2004; 2009).

91  
92 Despite the numerous examples of extension gradients in nature, analogue and numerical  
93 modellers mostly use constant along-strike deformation rates when simulating extensional  
94 tectonics and rift propagation (e.g. Withjack & Jamison 1986; Mart & Dauteuil 2000; Michon  
95 & Merle 2000; Van Wijk & Blackman 2005; Allken et al. 2011; 2012; Philippon et al. 2015;  
96 Ding & Li 2016). This is strictly only acceptable in cases where the Euler pole is sufficiently  
97 far away from the study area, so that rotational extension is locally near to orthogonal (e.g.  
98 Le Pourhiet et al. 2018). For situations in which the rotation pole is nearby, however,  
99 rotational motion needs to be taken into account (Smith 1993). The few authors who  
100 presented (analogue) models with along-strike extension rate variations focus on the

101 rotation of the Danakil Block associated with extension in the Afar (Souriot & Brun 1992,  
102 Fig. 2b), the continuation of the Havre Trough back-arc basin into the North Island of New  
103 Zealand (Benes & Scott 1996, Fig. 2h), rotational subduction rollback in the Pacific Kuril  
104 Basin (Schellart et al. 2002; 2003) and the Aegean (Kydonakis et al. 2015), as well as the  
105 opening of the South China Sea (Sun et al. 2009, Fig. 2i). Molnar et al. (2017; 2018; 2019)  
106 describe analogue models testing the influence of crustal and mantle weaknesses with  
107 various oblique trends relative to the extension direction on the evolution of propagating  
108 rifts.

109  
110 Recently, Mondy et al. (2018) used numerical models to test the differences between these  
111 two kinematic boundary conditions, showing the development of cylindrical or V-shaped  
112 basins for systems with constant along-strike extension and along-strike extension  
113 gradients, respectively. This paper complements their study by means of a systematic  
114 analogue modeling study of first-order rift propagation processes using simple analogue  
115 models including either (1) a traditional orthogonal extension set-up (involving a constant  
116 extension velocity along strike) or (2) a rotational extension set-up (involving an extension  
117 gradient along strike).

118  
119 The methodology applied for both set-ups is similar to that applied by Zwaan et al. (2019).  
120 We use top view photography and Digital Image Correlation (DIC) techniques to trace  
121 horizontal displacements at the surface of the models. Selected models are scanned with  
122 the use of X-ray computed tomography (XRCT or CT) techniques to reveal their 3D external  
123 and internal evolution in great detail. The model results are subsequently compared with  
124 previous models and natural examples.

125  
126  
127

## 128 2. Materials and methods

129

### 130 2.1 Model materials

131

132 We apply a brittle-viscous model layering, representative of either continental crust, or  
133 oceanic lithosphere (Fig. 3). The uppermost, brittle part of the model consists of a 4 cm  
134 thick layer of fine quartz sand ( $\phi = 60\text{-}250\ \mu\text{m}$ ) to simulate a 20 km upper continental crust  
135 or 7 km thick oceanic crust (Zwaan et al., 2018b). The sand is sieved from ca. 30 cm height  
136 into the experimental apparatus to maintain a constant sand density of ca.  $1560\ \text{kg/m}^3$  (e.g.  
137 Klinkmüller et al. 2016). During model construction, the sand is scraped and flattened at  
138 every cm thickness interval, causing slight density differences. This layering is often visible  
139 on CT images, but causes no artificial strain localization or differences in the resulting  
140 model structures. A 4 cm thick viscous basal layer represents a 20 km thick ductile lower  
141 crust or the uppermost 7 km of the oceanic lithospheric mantle. Our viscous material  
142 consists of a mixture of SGM-36 Polydimethylsiloxane (PDMS) silicone and a fine  
143 corundum sand (type NKF 120, with a specific density of  $3950\ \text{kg/m}^3$  and grain size of 88-  
144  $125\ \mu\text{m}$ , Panien et al. 2006; Carlo AG 2019). The resulting mixture has a density of ca.  
145  $1600\ \text{kg/m}^3$  and a near-Newtonian viscosity of ca.  $1.5 \cdot 10^5\ \text{Pa}\cdot\text{s}$  (Zwaan et al. 2018c).

146

### 147 2.2. Model set-up

148

149 For this study we use two experimental machines with fundamentally different basal  
150 kinematic boundary conditions (rotational vs. orthogonal extension). Both, however, apply  
151 the same basic method to induce primarily distributed extension in a brittle-ductile model  
152 layer (Zwaan et al. 2019). The model layering sits on top of an 8 cm thick RG 50  
153 Polyurethane foam block with a width of 35 cm (NB: in case of the rotational extension set-  
154 up, this width laterally decreases to 31 cm in order to accommodate the machine's  
155 differential deformation). In both machines, the foam is first compressed between their  
156 longitudinal sidewalls to reach the initial model width of 30 cm (Fig. 3a-d). On top of this  
157 compressed foam base, which itself rests on a fixed table that supports and allows the foam  
158 to move freely at its base (Fig. 3f), the viscous and brittle model materials are applied.  
159 During a model run, the sidewalls are driven apart by high-precision computer-controlled  
160 motors, causing near-uniform expansion in the foam (see supplementary data in Zwaan et  
161 al., 2020). This distributed extension is then transmitted to the overlying model materials.

162

163 In order to model orthogonal extension, both sidewalls of the 80 cm long orthogonal  
164 extension apparatus are moving apart perpendicularly (Fig. 3a, c), so that extension is  
165 constant along strike, as in most previous studies simulating extensional tectonics (e.g.  
166 Withjack & Jamison 1986; Michon & Merle 2000; Philippon et al. 2015). By contrast, the  
167 rotational extension set-up involves rotation of the sidewalls about a vertical axis to which  
168 they are attached via a connection at the base of the apparatus. The model is thus  
169 partitioned in a 65 cm long extensional and a 25 cm long contractional domain (Fig. 3b, d),  
170 a scaled configuration similar to the rotational tectonic setting in the Arctic (Fig. 2f). In both  
171 domains, deformation increases away from the rotation axis, where no deformation takes  
172 place. The far end of the rotational extension domain opens with the same velocity as the  
173 sidewalls in the orthogonal extension set-up (each moving at 4 mm/h resulting in 8 mm  
174 displacement per hour). The maximum shortening velocity on the other side of the rotation  
175 axis is accordingly 3.1 mm/h.

176

177 In order to localize externally applied extension into rifts in the centre of the model domain,  
178 we use thin “seeds” (1 cm thick, semi-cylindrical rods) of the PDMS/corundum sand mixture  
179 resting on top of the basal viscous layer (Fig. 3a, b, e, f). Here, deformation localizes since  
180 the overlying brittle layer is 25% thinner and therefore ca. 56% weaker (Figs. 3f, A1,  
181 Appendix A). Similar “seeds” are frequently used in both analogue and numerical models  
182 (e.g. Le Calvez & Vendeville 2002; Allken et al. 2011, 2012; Mondy et al. 2018) and act as  
183 linear weak zones simulating discrete weaknesses, in our case at the base of the crust,  
184 associated with e.g. old shear zones or sutures that are subsequently reactivated  
185 (Dyksterhuis et al. 2007). Such considerations are part of a wider discussion on how to  
186 implement structural weaknesses in tectonic models (Morley 1999; Zwaan et al. 2019). The  
187 seeds are placed along the central axis of the model and we differentiate between having  
188 no seed (reference set-up), or a seed over the whole model length.  
189

190 The model run duration amounts to 5 hours for a total of 40 mm of extension (8 mm/h) at  
191 the end of the model run (ca. 13% extension, given its 30 cm initial width, Fig. 3c, d). This  
192 extension velocity is chosen to prevent strong brittle-viscous coupling and associated  
193 distributed rifting effects, since we aim to analyze the development and propagation of a  
194 single well-constrained rift basin. No sedimentation is implemented in this study, which is  
195 permissible since we are not focusing on detailed rift-internal structures but on first-order  
196 tectonics processes that are not significantly affected when surface processes are excluded  
197 (Zwaan et al. 2018a). We completed 6 experiments in total, of which further details are  
198 listed in table 2.  
199

200

201

### 201 2.3. Model analysis

202

203 A thin (<1 mm thick) 4 x 4 cm surface grid of dark corundum sand visualized horizontal  
204 displacement on top view photographs taken every minute, allowing a primarily qualitative  
205 assessment of horizontal displacements. In addition, coffee powder sprinkled on the model  
206 surface provide a pattern on these digital images, enabling the use of digital image  
207 correlation (DIC, Adam et al., 2005; 2013 and references therein) techniques to quantify  
208 horizontal displacements and deformation of the model surface at high precision (<1 mm).  
209 We use commercial LaVision Davis 8 software applying DIC processing (more data and  
210 videos underlying this study can be found open access in Zwaan et al. 2020). Two models  
211 were rerun in a 64 slice Siemens Somatom Definition AS X-ray CT-scanner (Fig. 2f). We  
212 applied 30 min time steps for CT-scanning (a scan for every 4 mm of extension), yielding a  
213 coherent record of the 3D internal model evolution that can be analyzed in detail using  
214 OsiriX/Horos or other software packages. OsiriX/Horos also allows the extraction of model  
215 surfaces, basically properly georeferenced Digital Elevation Models (DEM), from the raw  
216 CT data. Subsequent data processing with the use of open source software (Meshlab and  
217 CloudCompare) enables an analysis of the uplift/subsidence evolution occurring in our  
218 models. DIC methods were also applied on along- and across-axis CT sections, providing  
219 further quantitative insights in the internal model deformation (Zwaan et al. 2020).  
220

221

222

223

224

225

226

## 227 2.4. Model scaling and natural analogues

228

229 For proper model scaling we calculate stress ratios ( $\sigma^*$ , convention:  $\sigma^* = \sigma_{\text{model}} / \sigma_{\text{nature}}$ ) with  
230 the following equation (Hubbert 1937; Ramberg 1981):  $\sigma^* = \rho^* \cdot h^* \cdot g^*$ , where  $\rho^*$ ,  $h^*$  and  $g^*$   
231 represent the density, length and gravity ratios respectively. The strain rate ratio  $\dot{\epsilon}^*$  is  
232 acquired from the stress ratio  $\sigma^*$  and the viscosity ratio  $\eta^*$  (Weijermars & Schmeling 1986):  
233  $\dot{\epsilon}^* = \sigma^* / \eta^*$ . Then, the velocity ratio  $v^*$  and time ratios  $t^*$  are derived with the following  
234 equations:  $\dot{\epsilon}^* = v^* / h^* = 1 / t^*$ . Natural lower continental crust has a wide viscosity range, ( $\eta =$   
235  $10^{19}$ - $10^{23}$  Pa·s, e.g. Buck 1991). Assuming an intermediate viscosity of  $10^{21}$  Pa·s commonly  
236 reported in literature (e.g. Shinevar et al. 2015) 1 hour in our models scales up to 0.84 My  
237 in nature. Our model extension velocity (8 mm/h) then translates to ca. 5 mm/y, close to  
238 typical extension rates in nature (Saria et al. 2014; ArRajehi et al. 2010, Fig. 2a, b). All  
239 scaling parameters are listed in Table 3.

240

241 In order to ensure dynamic similarity between the brittle model materials and their natural  
242 equivalents, we derive the ratio  $R_s$ , from the gravitational stress and cohesive strength or  
243 cohesion  $C$  (Ramberg 1981; Mulugeta 1998):  $R_s = \text{gravitational stress} / \text{cohesive strength} =$   
244  $(\rho \cdot g \cdot h) / C$ . We assume a cohesion of ca. 8 MPa for upper crustal rocks, which yields a  $R_s$   
245 value of 68 for both model and nature. Although this cohesion may be relatively low with  
246 respect to the ca. 20-40 MPa measured for most continental materials (e.g. Handin 1969;  
247 Jaeger & Cook 1976; Twiss & Moores 2007), it should be reasonable since the earth's crust  
248 is generally weakened by preceding tectonic and magmatic activity. For viscous materials,  
249 the Ramberg number  $R_m$  applies (Weijermars & Schmeling 1986):  $R_m = \text{gravitational}$   
250  $\text{stress} / \text{viscous strength} = (\rho \cdot g \cdot h^2) / (\eta \cdot v)$ . The  $R_m$  in our models and nature are both 75.  
251 Therefore we consider our models adequately scaled for continental rifting.

252

253 Alternatively, our models could represent an oceanic setting with the sand representing  
254 oceanic crust, the viscous layer replicating the uppermost part of a ductile lithospheric  
255 mantle and the underlying foam as the deeper parts of the lithospheric mantle. Accordingly,  
256 assuming a 7 km thick brittle oceanic crust and a lithospheric mantle viscosity of  $5 \cdot 10^{19}$   
257 Pa·s (mantle viscosities range between  $10^{18}$  and  $10^{21}$  Pa·s, Bürgmann & Dresen 2008, but  
258 should be relatively low for young hot lithosphere close to oceanic spreading centers), our  
259 model extension rates translate to ca. 12 mm/yr, similar to natural spreading rates (ca. 7-20  
260 mm/yr, Fig. 2a, b, e, ArRajehi et al. 2010; McClusky et al 2010). Furthermore, an  
261 intermediate cohesion of ca. 3 MPa for basalt (Schultz 1993) yields an  $R_s$  value of ca. 69,  
262 and a Ramberg number of 81 for the natural analogue. These values are very close to  
263 those of their model counterparts (68 and 75, respectively), indicating that our experiments  
264 are adequately scaled to simulate rifting of oceanic lithosphere as well.

265

266

267

268

### 269 3. Model results

#### 270 271 3.1. Top view and DIC surface deformation analysis

272  
273 We present an overview of final model surface views in Fig. 4, as well as of the finite stage  
274 DIC results in Fig. 5 and sequential DIC results in Fig. 6. For top views depicting the  
275 evolution of all models we refer the reader to Appendix C (Fig. C1) and the supplementary  
276 material (Zwaan et al. 2020). For description of the DIC results we apply an x-y surface  
277 coordinate system with the x-direction parallel to, and the y-direction perpendicular to the  
278 model length axis, respectively (see annotation in Figs. 5, 6). Profiles displaying quantified  
279 displacement are either oriented “across-strike” (i.e. aligned in y-direction) or “along-strike”  
280 (i.e. aligned in x-direction). Note that the displacement values in these profiles only  
281 represent the y-component of the total displacement vectors visible in map view (Fig. 5, 6),  
282 thus the component parallel to the extension direction. In this context, “northward”  
283 displacement is defined as positive and “southward” displacement as negative.

284  
285 Both model set-ups have in common that without a seed (Models O1 and R1), deformation  
286 localizes almost entirely along the longitudinal sidewalls (Figs. 4a, b, 5a, b, 6a, b). In the  
287 central part of the model domain minor distributed extension occurs (Fig. 6a, b). A minor  
288 fraction (<10%) of externally applied extension seems to localize at the short ends of the  
289 model domain (Fig. 6a, b) although no faulting can be observed by visual inspection. This  
290 local deformation is likely due to material being affected by the stretching rubber sidewalls.  
291 In the rotational experiment, we observe a similar small amount of effective extension and a  
292 slight gradient along-strike, as well as slightly increased deformation at the short ends of  
293 the model. Distributed across-strike contraction at the right-hand side of the rotational axis  
294 is consistent with externally applied shortening (Fig. 6b).

295  
296 A full model length seed generates rift localization along the central axis of the model in  
297 both set-ups (Fig. 4c, d, Fig. 5c, d). About 50% of externally applied extension is localized  
298 into the rift (Fig. 6c, d). In contrast to partially seeded models, extension varies only little  
299 along strike of the model domain in model O3, but still follows a slight bell shaped curve  
300 (Fig. 6c). Model R3 shows the typical linear decrease towards the propagating rift tip (Fig.  
301 6c). Orthogonal extension Model O3 (Fig. 4c, 5c) develops a continuous and symmetric rift  
302 basin along the full length of the model. This structure is formed early on (at  $t = 30$  min [ $e =$   
303  $4$  mm or  $1.3\%$  of extension], Figs. 6c, B2) and subsequently grows in width as extension  
304 progresses. The rotational extension equivalent model R3 also contains an early rift basin  
305 after some 30 min ( $e = 4$  mm or  $1.3\%$  of extension, Figs. 6d, C1). Yet this basin  
306 progressively propagates towards the rotation axis with on-going extension and (almost)  
307 reaches the axis at the end of the model run (Figs. 4j, 5j, C1j). Within the contractional  
308 domain on the other side of the rotation axis in model R3 and unique to this set of models, a  
309 thrust develops (Figs. 4d, 5d). This is clearly linked to the presence of a seed there, which  
310 localizes the distributed shortening previously observed in across-strike plots of Model R1  
311 (Fig. 6b, j).

312  
313  
314  
315  
316  
317  
318

### 319 3.2. 3D CT-based topography and structural analysis

320

321 Since the full-length seed experiments O2 and R2 formed the best-developed rift structures,  
322 they were rerun in the CT scanner as models O3 and R3, respectively (Table 2). The  
323 structures in Models O2 and R2 are very similar to those of O3 and R3 (Fig. B1),  
324 highlighting the reproducibility of this type of model. For experiment O3, we only scanned  
325 the 40 cm long central segment of the models, where any effects of the rubber sidewalls  
326 are negligible, thus best illustrating the general features of the model (Figs. 4c, 5c, 6c). On  
327 the other hand, the whole of Model R3 was scanned in order to capture the full extension  
328 gradient and the differential along-strike structural evolution as observed on the top view  
329 images and using DIC analysis (Figs. 4d, 5d, 6d). The 3D CT-derived snapshots in  
330 combination with serial cross-sections of horizontal CT sections illustrate the model internal  
331 evolution and the links with the model surface (Figs. 7, 8). Furthermore, the extraction of  
332 the model topography allows us to quantify the uplift and subsidence of the model surface  
333 (Fig. 9).

334

335 Early on in model O3 ( $t = \text{ca. } 30 \text{ min}$  [ $e = 4 \text{ mm}$  or  $1.3\%$ ]), a symmetric graben establishes  
336 itself above the full length of the seed (Figs. 7b, e, 9b) and the rift wedge starts subsiding  
337 between the rift boundary faults (Figs. 7e-f, 9b-c). After 120 min, the rift wedge starts to  
338 fragment and the viscous layer rises below the rift (Fig. 7g). The topography plots  
339 meanwhile show a general subsidence throughout the model, alongside the highly localized  
340 subsidence in the rift basin (Fig. 9d). With progressive extension, the rift wedge starts  
341 breaking up and the boundary faults start rotating away from the rift (Fig. 7g-h). At the end  
342 of the model run the viscous layer reaches the model surface through the remains of the  
343 broken-up rift wedge. Two major boundary faults, having rotated from their initial  $\text{ca. } 75^\circ$   
344 dip angles to  $\text{ca. } 60^\circ$  dip angles, flank the overall graben structure (Fig. 7i). In total, the rift basin  
345 undergoes some 25 mm of subsidence, whereas the model surface experiences an overall  
346 subsidence of  $\text{ca. } 5 \text{ mm}$  (Fig. 9e). The CT serial cross-sections illustrate the strong along-  
347 strike structural continuity previously recognized on top view images (Fig. 4e).

348

349 Similar to its orthogonal extension equivalent, a symmetric graben structure appears after  
350  $\text{ca. } 30 \text{ min}$  in rotational extension model R3 (Figs. 8b, e). However, the CT images illustrate  
351 how more developed rift structures develop in the outer part of the extension domain since  
352 the extension gradient causes increasingly more deformation and subsidence further away  
353 from the rotation axis. Yet the initially less evolved parts of the rift continue developing as  
354 well and subsequently attain the deformation stages the outer parts of the rift already went  
355 through (Fig. 8) Meanwhile the structures in these outer parts develop even further. The  
356 result is seen as the propagation of rift-related faulting from the outer to the inner part of the  
357 model. In the process, boundary fault angles decrease from  $\text{ca. } 75^\circ$  to  $\text{ca. } 65^\circ$  at the point  
358 furthest away from the rotation axis. As the model develops, the topography plots reveal  
359 how the rift (subsidence) propagates toward the rotation axis (Fig. 9g-h). Similar to Model  
360 O3, Model R3 also develops a general subsidence in the extensional part of the model,  
361 whereas strong subsidence ( $\text{ca. } 20 \text{ mm}$ ) remains restricted to the rift basin (Fig. 9j). On the  
362 opposite side of the rotation axis, we observe regional uplift and the development of a thrust  
363 after  $\text{ca. } 120 \text{ min}$  (Figs. 8g, 9h-i). This reverse fault, which is clearly rooted in the seed,  
364 strongly localized vertical motion (up to 5 mm uplift) toward the end of the model run (Fig.  
365 8j, 9j).

366

367 Although in 2D, the structures in models O3 and R3 are very similar (Figs 7-9), in 3D we  
368 observe a structural gradient in both time (compare any section in Fig 7 and its time

369 equivalent in Fig. 8) and space in Model R3 (e.g. compare section 1 from Fig. 7e with  
370 sections 2 and 3 from Fig. 8f and Fig. 8g, respectively, or section 1 from Fig 7h with section  
371 2 from Fig. 8i). By contrast, the features in Model O3 remain strictly cylindrical. These  
372 differences in along-strike maturity are associated with lateral flow of viscous material as  
373 visualized through DIC analysis on along-axis CT sections (Fig. 10). We find that Model O3  
374 does not show significant lateral displacement of viscous material (Fig. 10a), whereas the  
375 equivalent section in Model R3 displays clear viscous flow from the contractional to the  
376 extensional domain (Fig. 10b). However, we must stress that these results are only  
377 indicative since (viscous) material also moves across-axis (Zwaan et al. 2020), so that only  
378 a 3D assessment of the CT volume will provide a complete picture of internal deformation  
379 (e.g. Adam et al. 2013; Zwaan et al. 2018a).

380  
381

### 382 3.3. Strain partitioning and boundary effects

383

384 In the section above we describe how, seen in 2D, all our models with a seed develop a  
385 near-symmetric narrow rift structure, which in the case of the rotational set-up propagates  
386 towards the rotation axis (Figs. 4-6). However, we also observe significant strain partitioning  
387 between central rifts and faulting along the longitudinal model sidewalls (Figs. 4d, d, 5b, d,  
388 6b, d), or deformation focusing along the sidewalls (Figs. 4a, c, 5a, c, 6a, c). Such strain  
389 partitioning (or boundary effects) frequently occur in both analogue and numerical models  
390 of brittle-viscous systems and are hard if not impossible to prevent (Zwaan et al. 2019).  
391 They form integral parts of this type of experiments and can strongly affect model results,  
392 but are easily overseen.

393

394 DIC proves to be a powerful technique to quantify such effects and also reveals small,  
395 otherwise hidden influences of the confinement near the short sidewalls (Fig. 6). We  
396 interpret the decrease of localized extension towards the lateral sidewalls in Model O3 as a  
397 result of frictional drag along the uniformly stretching rubber sidewalls. This locally slows  
398 down and distributes the otherwise strongly localized deformation at the model surface (Fig.  
399 6e, g, i). The opposite seems to occur in Model O1: with no seed to focus deformation,  
400 most of the model surface behaves as a rigid block, yet the stretching rubber imposes a  
401 slight deformation along the short edges (Fig. 6a). These effects are less pronounced in the  
402 rotational extension model (Fig. 6d) possibly due to the use of foam rather than rubber at  
403 the short sidewalls (Fig. 3a, b), or due to overprinting by the extension gradient. Another  
404 minor feature is the occurrence of a slight component of lateral inward surface motion  
405 observed in various (orthogonal extension) models (Figs. 5, 6).

406

407

408

409

## 410 **4. Discussion**

411

### 412 4.1. General rift development

413

414 Seen in 2D, the development of symmetrical rift structures above the seeds in our models  
415 follows the same sequence of structural phases observed in previous studies with similar  
416 set-ups (e.g. Zwaan et al. 2018a; 2019). These models also generate initially steep rift  
417 boundary faults above the seed (Figs. 7e, 8e), followed by break-up of the rift wedge (Figs.  
418 7g, 8g) until the viscous layer is exhumed (Figs. 7i, 8i). The rotation of the rift boundary  
419 faults to shallower angles accommodates the strongly rising viscous layer (Zwaan et al.  
420 2018a). The sand seems to behave as rigid blocks during deformation, but when no seed is  
421 present, the DIC results show a hint of horizontal block rotation and minor distributed  
422 deformation (Fig. 6a, b), which is possibly due to minor brittle-viscous coupling. These  
423 effects are otherwise overshadowed by the dominant influence of a seed and the  
424 associated rift structure.

425

426 It is important to emphasize that our model results represent only one of the various generic  
427 rift modes that can occur, depending on factors such as the number, rheology and  
428 thickness of lithospheric layers (e.g. Brun 1999; Corti et al. 2003; Zwaan et al. 2019).  
429 Modeling efforts have for instance produced single rifts representing the same “narrow rift”  
430 settings as in our experiments (e.g. Michon & Merle 2000), “wide” rift systems with  
431 structures dispersed over larger areas (Benes & Davy 1996) as well as “core complex”  
432 development involving exhumation of ductile material (e.g. Brun et al. 2017). Lithospheric  
433 extension may furthermore be symmetric (pure shear, McKenzie 1978), asymmetric (simple  
434 shear, Wernicke 1985) or a combination of both. Other factors affecting rifting include multi-  
435 phase (oblique) extension (e.g. Keep & McClay 1997) thermal relaxation (Naliboff & Buiters  
436 2015), magmatism (Corti et al. 2003), the geometry of pre-existing structures (Dyksterhuis  
437 et al. 2007) and surface processes (e.g. Burov & Cloetingh 1997). However, since our main  
438 aim is to compare simple rift structures and their propagation in orthogonal and rotational  
439 extension settings, a full discussion of the above parameters is beyond the scope of this  
440 work.

441

442

443

## 444 4.2. Rift propagation

445

446 The continuous seed applied in Models O3 and R3 fully localizes deformation across the  
447 entire model and early on from the start of the model run (Figs 6ic d, 8, 9, C1). As  
448 orthogonal extension in model O3 is thus strongly localized, it instantaneously creates a  
449 continuous graben with nearly identical structures along its length and no rift propagation  
450 can occur (Figs. 7, 9). By contrast, the extension gradient in rotational extension models R3  
451 leads to the development of a (narrow) V-shaped graben with a clear structural gradient in  
452 both time and space (Fig. 8) so that rift-related subsidence propagates towards the less  
453 developed parts of the rift closer to the rotation axis (Fig. 9). Yet the rift structures in Model  
454 R3 are essentially the same as those in O3, but diachronous, in that they are at a different  
455 stage of development along-strike.

456

457 Since the set-ups for Models O3 and R3 are very similar to those of the numerical models  
458 by Mondy et al. (2018), who test both orthogonal extension and extension gradients in a  
459 continental setting that is localized by a central seed as well, they allow for an interesting  
460 comparison. The results of the early stages in both studies are remarkably similar: also  
461 Mondy et al. (2018) develop a continuous graben in orthogonal extension and a  
462 propagating rift when extension is “rotational” with a similar gradient development stages  
463 along-strike. An important difference however, is that their numerical models can  
464 accommodate much more extension (up to 60% versus our ca. 13%), including continental  
465 break up and mantle exhumation leading to a higher-angled V-shape in the oceanic  
466 spreading stage, reminiscent of the the well-developed V-shapes found in nature (Fig. 2,  
467 10b). Furthermore, our experimental boundary conditions seem very similar to those  
468 adopted by Mondy et al. (2018), but differ slightly in a fundamental way; our extension  
469 directions follow small circles around the rotation pole (Fig. 2d’), whereas Mondy et al.  
470 (2018) keep extension directions orthogonal to the model axis at all times (similar to in our  
471 orthogonal extension models, Fig. 2c’), but impose an extension gradient numerically. Both  
472 are in fact compromises with respect to plate tectonics on a globe (Fig. 3c), yet the  
473 relatively small amounts of extension should avoid significant discrepancies between both  
474 model series, and nature. Therefore, the overall results of both works are very compatible  
475 and highlight that structural gradients are an integral part of rift propagation and V-shape  
476 basin development (Figs. 1b, 10a, b).

477

478 When comparing our results with other analogue studies of rotational extension, we find  
479 large-scale similarities. Also Molnar et al. (2017, 2018, 2019) show generally propagating  
480 rift systems, although sometimes these involve various lateral rift-basins, rather than the  
481 single structure in our models. This is most likely due to their choice for a lithospheric-scale  
482 set-up (see also 4.1). When introducing (oblique) heterogeneities in the simulated crust and  
483 mantle, Molnar et al. (2017, 2018, 2019) find that rift structures are deflected, sometimes  
484 leading to highly complex tectonic patterns. Benes & Scott (1996) present well-developed  
485 rift propagation, but also show the effects of heterogeneities, in their case the effect of an  
486 oceanic rift entering a continental domain and being diffused and sometimes reoriented.  
487 Indeed, other modeling work shows that deformation in front of a propagating rift tip may be  
488 distributed over a wider area when entering into a more competent domain (Van Wijk &  
489 Blackman 2005; Allken et al. 2011, 2012; Le Pourhiet et al. 2018, Fig. 11d). Sun et al.  
490 (2009) obtain well-defined propagating rifts in their lithospheric-scale models, but their  
491 choice of plate boundary geometry also leads to oblique faulting. Furthermore, their  
492 application of “rigid massifs” causes deflection of model structures around these obstacles.

493

#### 494 4.3. Insights from topography analysis

495

496 The topography analysis of Models O3 and R3 illustrates the formation of a rift depocenter  
497 and, in the case of Model R3, its propagation toward the rotation axis, as well as a general  
498 subsidence in the extensional domain (Fig. 9). This general subsidence is due to the  
499 extending and simultaneously thinning viscous layer, similar to the behavior of the lower  
500 crust in rifted margin settings (Huisman et al. 2001), whereas the sand principally forms  
501 rigid blocks that do not undergo significant thinning (Zwaan et al. 2018a, Fig. 6). By  
502 contrast, the contractional domain either remains at a stable level or is uplifted above the  
503 pop-up structure (yellow and orange-red in Fig. 9, respectively). However, such vertical  
504 motions may be counteracted by various processes in nature (e.g. magmatism and doming  
505 due to mantle plume emplacement, Underhill & Partington 1993; Moucha & Forte 2011),  
506 which are not included in our experiments.

507

508 However, the presence of a viscous layer induces isostatic effects. DIC analysis of CT data  
509 from Model O3 does not reveal important along-axis displacement of material, yet Model R3  
510 shows along-axis flow of viscous material (Figs. 9f-j, 10b), indicating interaction between  
511 the model domains on both sides of the rotation axis. Pressure gradients due to along-strike  
512 variations in topography (and absent in model O3) are likely to cause this lateral flow,  
513 especially in propagating rift branches as also observed in previous models (Zwaan et al.  
514 2018a). Similar flow of lower crustal material is well documented (e.g. McKenzie et al. 2000;  
515 Little et al. 2007; Dewei 2008) and is also present in the numerical models by Mondy et al.  
516 (2018). Furthermore, Le Pourhiet et al. (2018) have shown that such variations in  
517 topography and crustal thickness may halt rift propagation, highlighting the importance of  
518 the third dimension in tectonic systems.

519

#### 520 4.4. Strain partitioning and boundary effects

521

522 Ding & Li (2016) introduce similar rigid massifs as Sun et al. (2009) in their crustal-scale,  
523 orthogonal extension models and argue that these cause rift propagation. Furthermore, the  
524 authors insist that rotational extension would lead to simultaneous break-up along the  
525 whole rift axis. This is however in stark contrast with our models since such “clean” instant  
526 break-up should only occur in the rather unrealistic case of a completely rigid plate tectonic  
527 system without any ductile influences (Bosworth 2015). We however suspect that some  
528 differential strain partitioning between the main rift and other parts of the model has taken  
529 place in the Ding & Li (2016) models, of which some examples can be found in the  
530 supplementary materials (Zwaan et al. 2020). This effect is also very clearly present in the  
531 models by Mart & Dauteuil (2000) (see also Fig. 12), and illustrates how even in orthogonal  
532 extension settings, rift propagation is associated with rotation.

533

534 Such strain partitioning thus strongly affects model results and can have important  
535 implications when for instance studying how fault systems develop in detail (Jackson et al.  
536 2017; Rotevatn et al. 2018). Detailed fault evolution analysis on analogue models such as  
537 those by Schlagenhaut et al. (2008) may be fundamentally flawed if boundary effects are  
538 not considered; apparent fault propagation may simply be due to deformation focusing  
539 elsewhere in the model (Fig. 12). We therefore urge modelers to describe and quantify  
540 boundary effects in their work and to provide all relevant boundary conditions. Only by  
541 doing so, a proper assessment and comparison of results from different experimental  
542 studies can be possible (Zwaan et al. 2019).

543

544  
545  
546  
547  
548  
549  
550  
551  
552  
553  
554  
555  
556  
557  
558  
559  
560  
561  
562  
563  
564  
565  
566  
567  
568  
569  
570  
571  
572  
573  
574  
575  
576  
577  
578  
579  
580  
581  
582  
583  
584  
585  
586  
587  
588  
589  
590  
591  
592  
593

## 4.5. Comparison with natural analogues

### 4.5.1. Regional-scale examples of rift-propagation

The situation in the Arctic represents the best example of a rotational tectonic system with an extension domain involving an extension rate gradient along the oceanic Gakkel Ridge and contraction in the Siberian Chersky Range, with an Euler pole near the Laptev Margin (Fig. 2f). The natural example bears clear resemblance to our model results (Figs. 4d, 5d, 6d, 8, 9d). Yet there are some differences between model and nature. The Gakkel Ridge is situated in an oceanic basin, and the Chersky Range is continental, whereas our model consists of a continuous brittle layer that must represent either continental or oceanic crust (see section 2.4). The ocean-continent transition is marked by the Severnyi Transfer fault where the strongly localized deformation along the Gakkel ridge shifts to diffuse deformation on the Laptev Margin (e.g. Van Wijk & Blackman 2005; Franke & Hinz 2009, Fig. 2f). A similar situation can be found in New Zealand, including compression on the other side of the Euler pole (e.g. Benes & Scott 1996, Seebeck et al. 2014, Fig. 2h). Yet although the ocean-continent transition locally complicates rift propagation structures in both cases, the general picture agrees with our rotational model.

The Red Sea forms a narrow oceanic basin between the African and Arabian plate (Fig. 2a). Continental rifting started around ca. 23 Ma (e.g. Bosworth 2015), followed by continental break-up around 5 Ma (e.g. Augustin et al. 2014), due to the rotation of the Arabian plate about a pole situated in Egypt (Bellahsen et al. 2003; ArRajehi et al. 2010, Fig. 2a). The original “nodal” break-up model for the Red Sea involves simultaneous deformation throughout the rift zone due to locally rising asthenosphere bulges (Courtilot 1982; Ligi et al. 2012; Fig. 11c). This scenario is most likely incorrect as the Red Sea bathymetry (on which the node model is based) is strongly affected by slumping sediments giving a false impression of “nodes” (Augustin et al. 2014). Instead, the Red Sea probably formed by simple rift propagation due to its rotation-induced opening (Figs. 2a, 10a, b, Augustin et al. 2014). Yet some analogue studies report node-like rift development (e.g. Sun et al. 2009; Ding & Li 2016; Molnar et al. 2017), suggesting that further research on the node model may be required. Moreover, the Red Sea represents the extension of the Gulf of Aden basin, both of which on a larger scale form part of a full rotational tectonic system as the Arabian plate collides with the Eurasian plate to its NE, although perhaps not as obvious as in the Arctic case (Fig. 2a, f). This, in combination with local rheology of the lithosphere (see section 2.4), indicates a very good first-order correlation with our model results.

Two other examples of rift propagation occur in the Woodlark Basin offshore Papua New Guinea (Fig. 2g) and the Pacific Galapagos Rise (Fig. 2e), both presented in the numerical modeling study by Mondy et al. (2018). As discussed above, their models are in good agreement with our results and produce similar V-shaped basins. Small-scale differences are most likely due to the inclusion of mantle flow, which may assist rift propagation, leading to the formation of an over-deepened through at the rift tip and interestingly enough, can cause phases of inversion. Both these large- and small-scale features are observed in the Woodlark Basin and Galapagos Rise (Taylor et al. 1995; Floyd et al. 2002, Fig. 2e, g). Whereas the former is a V-shaped basin developing into continental crust (Taylor et al. 1999), the latter example is fully oceanic, not completely corresponding to the initially continental Mondy et al. (2018) model. But such a comparison may be permissible, as also

594 our set-ups can be applied to simulate both continental and oceanic settings (see section  
595 2.4). The Galapagos Rise also best fits the simple V-shape of our rotational extension  
596 model (Fig. 2e), whereas the structure of the Woodlark Basin is rather complex in detail,  
597 involving various individual rift segments (e.g. Taylor et al. 1999, Fig. 11d). Yet, the  
598 compressional setting in Papua New Guinea, on the other side of the rotation axis may  
599 suggest a full rotational tectonic system (Fig. 2g), although local tectonics are complex (e.g.  
600 Holm et al. 2016). The currently inactive Coral Sea basin to its south was formed in a  
601 similar setting during the Paleocene (Fig. 2g) and also propagated westward into  
602 continental crust (of the Australian plate, Weissel & Watts 1979; Bulois et al. 2018a, Fig.  
603 2g).

604  
605 The SW-NE oriented South China sub basin (SCSB) provides another example of a well-  
606 developed V-shaped basin underlain by oceanic crust (Savva et al. 2014, Fig. 2i). The  
607 basin contains an extension gradient with the most developed segments to the NE (Ding et  
608 al. 2016). Rifting and breakup started in the Oligocene and propagated from NE to SW  
609 (Savva et al. 2014; Ding et al. 2016), very much in line with our rotational extension models.  
610 Yet Le Pourhiet et al. (2018) propose a scenario involving orthogonal extension for the  
611 SCSB in which additional rift-parallel shortening prevents an otherwise continuous rift from  
612 developing. Although the details of rift development are thus debated, the general features  
613 and structural history of the SCSB are in general agreement with our model results (Sun et  
614 al. 2009; Savva et al. 2014).

615  
616

#### 617 4.5.2. Local-scale examples of rift propagation

618

619 The Porcupine Basin offshore Ireland is one of the various smaller V-shaped basins along  
620 the NE Atlantic margin (Péron-Pinvidic & Manatschal 2010, Fletcher et al. 2013, Fig. 2d).  
621 The basin propagated from south to north during the opening of the North Atlantic in Late  
622 Jurassic-Early Cretaceous times (Bulois et al. 2018b; Chen et al. 2018), as indicated by the  
623 general wedge shape of its syn-rift fault patterns and sediments, and a southward increase  
624 in stretching factor (Tate 1993). At the southern limits of the basin, where the thickest syn-  
625 rift sediments occur, extreme crustal stretching is observed and even oceanic crust may  
626 have formed (Prada et al. 2018; Chen et al. 2018). The structures of the Porcupine Basin  
627 are in general agreement with our model results, but we must point out that northern  
628 propagation of the basin was halted and deflected by the strong Caledonian basement.

629

630 In East Africa, the Main Ethiopian Rift (MER) is another relevant natural analogue (Fig. 2a,  
631 c). It developed as a late third arm of the Afar triple junction around 11 Ma (Wolfenden et al.  
632 2004) and is thought to have propagated southward through the Ethiopian Highlands  
633 towards the other segments of the East African Rift System (Bonini et al. 2005; Brune et al.  
634 2017, Fig. 2a). Extension rates increase from north to south (Saria et al. 2014), and in its  
635 current form the MER represents a clear structural gradient from young continental rifting in  
636 the southern MER, to a mature rift stage in its northern sectors, where it funnels out into  
637 Afar (e.g. Corti 2009, Ebinger et al. 2010, Fig. 2c). Yet except for this funneling-out in the  
638 north, the MER generally does not show a distinct northward widening that should  
639 accommodate its increasing maturity. A key factor may be the relative extension direction,  
640 which changes due to the curving rift trend: extension obliquity (angle  $\alpha$ ) is ca.  $0^\circ$  in the  
641 southern MER but increases to ca.  $45^\circ$  in the northern MER (Agostini et al. 2011, Fig. 2c).  
642 Since rifts forming in oblique extension regimes are narrower than those in orthogonal

643 extension conditions (e.g. Tron & Brun 1991; Zwaan et al. 2016), this northward increase in  
644 extension obliquity could account for the rather constant rift width.

645

646 A final comparison can be made with the Afar Depression in East Africa, which itself is part  
647 of the larger Red Sea-Gulf of Aden rift system (Figs. 2a, b). Here continental break-up is  
648 currently taking place (e.g. Corti et al. 2015) as the Danakil Block rotates away from Africa  
649 in an anticlockwise fashion (e.g. Souriot & Brun 1982; McClucksky et al. 2010; Fig. 2b). Our  
650 models predict that the most developed parts of the Afar rift occur in the south, where most  
651 extension has taken place. Yet the opposite is true as the thinnest crust is situated in the  
652 Danakil Depression (15 km, against 25 km to the south, Ebinger et al. 2010; Bastow & Keir  
653 2011, Fig. 2b). This discrepancy can perhaps be explained by massive lower crustal  
654 intrusion replenishing the stretching crust (Stab et al. 2016). Yet the Afar rift configuration is  
655 diametrically opposite to our model results and highlights the necessity to consider  
656 additional parameters when interpreting experimental data.

657

658

659 **5. Conclusion**

660

661 We ran analogue tectonic experiments to assess the differences in the development and  
662 propagation of rifts under orthogonal extension and rotational extension conditions,  
663 providing the following insights:

664

665 • Our models provide a good first-order insight into large-scale rift development: under  
666 orthogonal extension conditions, a rift basin with constant and synchronous along-  
667 strike features develops, whereas rotational extension leads to diachronous rift  
668 development and an along-strike structural gradient.

669

670 • Rotational extension is shown to be a key factor for rift propagation and the  
671 development of V-shaped basins, highlighting the importance of considering the third  
672 dimension in tectonic systems. Any cases of rift propagation in orthogonal extension  
673 models are likely due to differential strain partitioning.

674

675 • Our rotational tectonic models provide direct evidence of interaction between the  
676 extensional and contractional domain on either side of the rotation axis, manifested  
677 by lateral flow of viscous material due to pressure gradients.

678

679 • Stretching of the lower crustal analogue is shown to cause regional subsidence, with  
680 rift basins representing intense local subsidence, yet in nature we should expect  
681 isostatic responses of the mantle and lithosphere,

682

683 • The above points are first-order, still our model results are in good agreement with  
684 various natural examples, as well as previous analogue and numerical models.  
685 However, various geological parameters such as structural inheritance, (oblique)  
686 orientation of the rift system, lithospheric layering and rheology, magmatism and  
687 mantle plume emplacement are known to potentially affect the structural style of  
688 developing rift systems and their propagation.

689

690 • We furthermore urge modelers to report boundary effects in their models, as these  
691 may have a major influence on e.g. fault propagation, which, if not accounted for,  
692 may lead to incorrect conclusions.

693

694

695

696

## 697 **6. Acknowledgements**

698

699 We would like to express our gratitude to Nicole Schwendener for assisting us with the CT-  
700 scanning, Kirsten Busse for helping us with topography analysis, Marco Herwegh for  
701 providing funds to upgrade the orthogonal extension apparatus and to construct the new  
702 rotational tectonic apparatus. We also thank the engineers from IPEK Rapperswil (Theodor  
703 Wüst, Reto Gwerder, Rudolf Kamber, Michael Ziltener, Christoph Zolliker and Claude Grau)  
704 for realizing the improvements to the existing machine and the design and construction of  
705 the new rotational tectonic apparatus. Fruitful discussions with Timothy Schmid and  
706 Sascha Brune helped improve our model analysis. We are grateful to Fernando Ornelas  
707 Marques, Luke Mondy, Guillaume Duclaux and an anonymous reviewer for their helpful and  
708 constructive comments. The Berne University Science Foundation contributed generously  
709 to the new machine as well and the project in general was funded by the Swiss National  
710 Science Foundation (grant no. 200021\_147046/1). We thank Kirsten Elger from the GFZ  
711 Data Services for publishing the data underlying this study (Zwaan et al. 2020).

712

713

## 714 **Appendix A**

715

716 In order to calculate the difference in brittle strength between the standard sand layer and  
717 the sand above the seed (i.e. the difference in surface of the respective triangles made by  
718 the strength profile, see also Fig. 3f), we apply the law of cosines (Fig. A1):

719

$$720 \quad o/a = \tan(c) \quad (\text{eq. A1})$$

721

722 where (o) and (a) represent the opposite and adjacent sides of the triangle.

723

724 In addition, we use the formula for the surface area of a triangle:

725

$$726 \quad A = \frac{1}{2} h b \quad (\text{eq. A2})$$

727

728 Where (h) and (b) represent the height (or depth) and base length, and (A) the surface area  
729 of the triangle, respectively.

730

731 Since in our system (a) = (h) and (o) = (b), we can rewrite equation A2 as:

732

$$733 \quad A = \frac{1}{2} a^2 \tan(c) \quad (\text{eq. A3})$$

734

735 For calculating the surface ratio of two triangles with the same angles (c), but different  
736 dimensions (i.e. triangles x and y), we use the following formula:

737

$$738 \quad \text{Strength ratio} = A_x/A_y = (\frac{1}{2} a_x^2 \tan(c)) / (\frac{1}{2} a_y^2 \tan(c)) = a_x^2 / a_y^2 \quad (\text{eq. A4})$$

739

740 In our models, since  $a_x = 3$  cm (above seed) and  $a_y = 4$  cm (away from the seed), the  
741 strength ratio is between both cases is 56%.

742

743

744

745 **Appendix B**

746

747 In Fig. B1, the surface photographs of models O2 and O3, compared to their CT-scanned  
748 counterpart, illustrate the reproducibility of our model results

749

750 **Appendix C**

751

752 Fig. C2 provide an overview of the surface evolution and DIC map view results of models  
753 O3 and R3. Note that the cumulative horizontal displacement plotted on the map view  
754 images is given as across-strike (i.e. in y-direction). The triangles along the margins of the  
755 images indicate the locations of sections along which deformation is plotted in Fig. 6.

756

757

758 **Data availability**

759

760 Animations and digital image correlation data presented in this study are available as an  
761 open access data publication on the GFZ Data Service: Zwaan et al. (2020).

762 **Temporary link (data publication is not finalized yet):** [http://pmd.gfz-  
763 potsdam.de/panmetaworks/review/727b14a07cbea4b20911d443b6586d822f9270554c78f6  
764 6186d107ffb2bf20d0](http://pmd.gfz-potsdam.de/panmetaworks/review/727b14a07cbea4b20911d443b6586d822f9270554c78f66186d107ffb2bf20d0)

765

766

767

768 **References**

769

770 Adam, J., J.L. Urai, B. Wieneke, O. Oncken, K. Pfeiffer, N. Kukowski, J. Lohrmann, S. Hoth,  
771 W. van der Zee, J. Schmatz, (2005), Shear localisation and strain distribution during  
772 tectonic faulting - New insights from granular-flow experiments and high-resolution optical  
773 image correlation techniques, *Journal of Structural Geology*, 27(2), 183-301.  
774 <http://doi.org/10.1016/j.jsg.2004.08.008>

775

776 Adam, J., Klinkmüller, M., Schreurs, G., Wieneke, B. 2013. Quantitative 3D strain analysis  
777 in analogue experiments simulating tectonic deformation: Integration of X-ray computed  
778 tomography and digital volume correlation techniques. *Journal of Structural Geology* 55,  
779 127-149.  
780 <http://dx.doi.org/10.1016/j.jsg.2013.07.011>

781

782 Agostini, A., Bonini, M., Corti, G., Sani, F., Mazzarini, F. 2011. Fault architecture in the Main  
783 Ethiopian Rift and comparison with experimental models: Implications for rift evolution and  
784 Nubia–Somalia kinematics. *Earth and Planetary Science Letters* 301, 479-492.  
785 <https://doi.org/10.1016/j.epsl.2010.11.024>

786

787 Allemand, P., Brun, J.-P. 1991. Width of continental rifts and rheological layering of the  
788 lithosphere. *Tectonophysics* 188, 63-69.  
789 [https://doi.org/10.1016/0040-1951\(91\)90314-I](https://doi.org/10.1016/0040-1951(91)90314-I)

790

791 Allken, V., Huismans, R.S., Thieulot, C. 2011. Three-dimensional numerical modeling of  
792 upper crustal extensional systems. *Journal of Geophysical Research* 116, B10409.  
793 <https://doi.org/10.1029/2011JB008319>

794

795 Allken, V., Huisman, R.S., Thieulot, C. 2012. Factors controlling the mode of rift interaction  
796 in brittle-ductile coupled systems: A 3D numerical study. *Geochemistry, Geophysics,*  
797 *Geosystems* 13, Q05010.  
798 <https://doi.org/10.1029/2012GC004077>  
799

800 ArRajehi, A., McClusky, S., Reilinger, R., Daoud, M., Alchalbi, A., Ergintav, S., Gomez, F.,  
801 Sholan, J., Bou-Rabee, F., Ogubazghi, G., Haileab, B., Fisseha, S., Asfaw, L., Mahmoud,  
802 S., Rayan, A., Bendik, R., Kogan, L. 2010. Geodetic constraints on present-day motion of  
803 the Arabian Plate: Implications for Red Sea and Gulf of Aden rifting. *Tectonics* 29, TC3011.  
804 <https://doi.org/10.1029/2009TC002482>  
805

806 Augustin, N., Devey, C.W., Van der Zwan, F.M., Feldens, P., Tominaga, M., Bantan, R.A.,  
807 Kwasnitschka, T. 2014. The rifting to spreading transition in the Red Sea. *Earth and*  
808 *Planetary Science Letters* 395, 217-230  
809 <https://doi.org/10.1016/j.epsl.2014.03.047>  
810

811 Bastow, I.D., Keir, D. 2011. The protracted development of the continent–ocean transition  
812 in Afar. *Nature Geoscience* 4.  
813 <https://doi.org/10.1038/NGEO1095>  
814

815 Benes, V., Scott, S.D., Binns, R.A. 1994. Tectonics of rift propagation into a continental  
816 margin: Western Woodlark Basin, Papua New Guinea. *Journal of Geophysical Research* 99  
817 (B3), 4439-4455.  
818 <https://doi.org/10.1029/93JB02878>  
819

820 Benes, V., Scott, S.D. 1996. Oblique Rifting in the Havre Trough and Its Propagation into  
821 the Continental Margin of New Zealand: Comparison with Analogue Experiments. *Marine*  
822 *Geophysical Researches* 18, 189-201.  
823 <https://doi.org/10.1007/BF00286077>  
824

825 Benes, V., Davy, P., 1996. Modes of continental lithospheric extension: experimental  
826 verification of strain localization processes. *Tectonophysics* 254, 69–87.  
827 [https://doi.org/10.1016/0040-1951\(95\)00076-3](https://doi.org/10.1016/0040-1951(95)00076-3)  
828

829 Bellahsen, N., Facenna, C., Funicello, F., Daniel, J.M., Jolivet, L. 2003. Why did Arabia  
830 separate from Africa? Insights from 3-D laboratory experiments. *Earth and Planetary*  
831 *Science Letters* 216, 365-381.  
832 [https://doi.org/10.1016/S0012-821X\(03\)00516-8](https://doi.org/10.1016/S0012-821X(03)00516-8)  
833

834 Beyene, A., Abdelsalam, M.G., 2005. Tectonics of the Afar Depression: A review and  
835 synthesis. *Journal of African Earth Sciences*, 41, 41-59.  
836 <https://doi.org/10.1016/j.jafrearsci.2005.03.003>  
837

838 Bonini, M., Corti, G., Innocenti, F., Manetti, P., Mazzarini, F., Abebe, T. Pecskey, Z. 2005.  
839 Evolution of the Main Ethiopian Rift in the frame of Afar and Kenya rifts propagation.  
840 *Tectonics* 24, TC1007.  
841 <https://doi.org/10.1029/2004TC001680>  
842

843 Bosworth, W. 2015. Geological Evolution of the Red Sea: Historical Background, Review,  
844 and Synthesis. In: Rasul N., Stewart I. (eds) The Red Sea. Springer Earth System  
845 Sciences. Springer, Berlin, Heidelberg.  
846 [https://doi.org/10.1007/978-3-662-45201-1\\_3](https://doi.org/10.1007/978-3-662-45201-1_3)  
847

848 Brun, J.-P. 1999. Narrow rifts versus wide rifts: inferences for the mechanics of rifting from  
849 laboratory experiments. Philosophical Transactions of the Royal Society London A 357,  
850 695-712.  
851 <https://doi.org/10.1098/rsta.1999.0349>  
852

853 Brun, J.-P., Sokoutis, D., Tirel, C., Gueydan, F., Van den Driessche, J., Beslier, M.-O. 2017.  
854 Crustal versus mantle core complexes. Tectonophysics 746, 22-45.  
855 <http://dx.doi.org/10.1016/j.tecto.2017.09.017>  
856

857 Brune, S., Corti, G., Ranalli, G. 2017. Controls of inherited lithospheric heterogeneity on rift  
858 linkage: Numerical and analog models of interaction between the Kenyan and Ethiopian  
859 rifts across the Turkana depression. Tectonics 36, 1767–1786.  
860 <https://doi.org/10.1002/2017TC004739>  
861

862 Buck, W.R. 1991. Models of Continental Lithospheric Extension. Journal of Geophysical  
863 Research 96, 20,161-20,178.  
864 <https://doi.org/10.1029/91JB01485>  
865

866 Bulois, C., Pubellier, M., Chamot-Rooke, N., Delescluse, M. 2018a. Successive Rifting  
867 Events in Marginal Basins: The Example of the Coral Sea Region (Papua New Guinea).  
868 Tectonics 37, 3–29.  
869 <https://doi.org/10.1002/2017TC004783>  
870

871 Bulois, C., Pubellier, M., Chamot-Rooke, N., Watremez, L. 2018b. From orogenic collapse  
872 to rifting: A case study of the northern Porcupine Basin, offshore Ireland. Journal of  
873 Structural Geology 114, 139-162.  
874 <https://doi.org/10.1016/j.jsg.2018.06.021>  
875

876 Bürgman, R., Dresen, G., 2008. Rheology of the Lower Crust and Upper Mantle: Evidence  
877 from Rock Mechanics, Geodesy, and Field Observations. Annual Review of Earth and  
878 Planetary Sciences 36, 531-67.  
879 <https://doi.org/10.1146/annurev.earth.36.031207.124326>  
880

881 Burov, E., Cloetingh, S. 1997. Erosion and rift dynamics: new thermomechanical aspects of  
882 post-rift evolution of extensional basins. Earth and Planetary Science Letters 150, 7-26.  
883 [https://doi.org/10.1016/S0012-821X\(97\)00069-1](https://doi.org/10.1016/S0012-821X(97)00069-1)  
884

885 Burov, E., Poliakov, A. 2001. Erosion and rheology controls on synrift and postrift evolution:  
886 verifying old and new ideas using a fully coupled numerical model. Journal of Geophysical  
887 Research 106 (B8), 16,461–16,481.  
888 <http://dx.doi.org/10.1029/2001JB000433>.  
889

890 Carlo AG (Carlo Bernasconi AG, Switzerland) 2019.  
891 Company website: [www.carloag.ch](http://www.carloag.ch)  
892

893  
894  
895  
896  
897  
898  
899  
900  
901  
902  
903  
904  
905  
906  
907  
908  
909  
910  
911  
912  
913  
914  
915  
916  
917  
918  
919  
920  
921  
922  
923  
924  
925  
926  
927  
928  
929  
930  
931  
932  
933  
934  
935  
936  
937  
938  
939  
940  
941  
942

Chen, C., Watremez, L., Prada, M., Minshull, T.A., Edwards, R.A., O'Reilly, B.M., Reston, T.J., Wagner, G., Gaw, V., Klaeschen, D., Schannon, P.M. 2018. From Continental Hyperextension to Seafloor Spreading: New Insights on the Porcupine Basin From Wide - Angle Seismic Data. *JGR: Solid Earth*  
<https://doi.org/10.1029/2018JB016375>

Corti, G., 2009. Continental rift evolution: From rift initiation to incipient break-up in the Main Ethiopian Rift, East Africa. *Earth-Science Reviews*, 96, 1-53.  
<https://doi.org/10.1016/j.earscirev.2009.06.005>

Corti, G., Bonini, B., Conticelli, S., Innocenti, F., Manetti P., Sokoutis, D. 2003. Analogue modelling of continental extension: a review focused on the relations between the patterns of deformation and the presence of magma.  
[https://doi.org/10.1016/S0012-8252\(03\)00035-7](https://doi.org/10.1016/S0012-8252(03)00035-7)

Corti, G., Bastow, I.D., Keir, D., Pagli, C., Baker, E., 2015. Rift-Related Morphology of the Afar Depression. In: Billi, P. (ed.) *Landscapes and Landforms of Ethiopia, World Geomorphological Landscapes*. Springer Science+Business Media, Dordrecht, 251-274.  
[https://doi.org/10.1007/978-94-017-8026-1\\_15](https://doi.org/10.1007/978-94-017-8026-1_15)

Courtillot, V. 1982. Propagating rifts and continental breakup. *Tectonics* 1, 239-250.  
<https://doi.org/10.1029/TC001i003p00239>

Demets, C., Gordon, R.G., Angus, D.F. 2010. Geologically current plate motions. *Geophysical Journal International* 181, 1-80.  
<https://doi.org/10.1111/j.1365-246X.2009.04491.x>

Dewei, L. 2008. Continental Lower-crustal Flow: Channel Flow and Laminar Flow. *Earth-Science Frontiers* 15, 130-139.  
[https://doi.org/10.1016/S1872-5791\(08\)60065-2](https://doi.org/10.1016/S1872-5791(08)60065-2)

Dick, H.J.B., Lin, J., Schouten, H. 2003. An ultra-slow spreading class of oceanic ridge. *Nature* 426, 405-412.  
<https://doi.org/10.1038/nature02128>

Ding, W., Li, J. 2016. Propagated rifting in the Southwest Sub-basin, South China Sea: Insights from analogue modelling. *Journal of Geodynamics* 100, 71-86.  
<https://doi.org/10.1016/j.jog.2016.02.004>

Ding, W., Li, J., Clift, P.D., IODP Expedition 349 scientists. 2016. Spreading dynamics and sedimentary process of the Southwest Sub-basin, South China Sea: Constraints from multi-channel seismic data and IODP Expedition 349. *Journal of Asian Earth Sciences* 115, 97-113.  
<http://dx.doi.org/10.1016/j.jseaes.2015.09.013>

Drachev, S.S., Savostin, L.A., Groshev, V.G., Bruni, I.E. 1998. Structure and geology of the continental shelf of the Laptev Sea, Eastern Russian Arctic. *Tectonophysics* 298, 357-393.  
[https://doi.org/10.1016/S0040-1951\(98\)00159-0](https://doi.org/10.1016/S0040-1951(98)00159-0)

943 Dyksterhuis, S., Rey, P., Müller, R.D., Moresi, L. 2007. Effects of initial weakness on rift  
944 architecture. In: Karner, G.D., Manatschal, G., Pinheiro, L.M. (eds.) *Imaging, Mapping and*  
945 *Modelling Continental Lithosphere Extension and Breakup*. Geological Society, London,  
946 Special Publications 282, 443–455.  
947 <https://doi.org/10.1144/SP282.18>  
948

949 Ebinger, C., Ayele, A., Keir, D., Rowland, J., Yirgu, G., Wriqth, T., Belachew, M., Hamling,  
950 I., 2010. Length and Timescales of Rift Faulting and Magma Intrusion: The Afar Rifting  
951 Cycle from 2005 to Present. *Annual Review of Earth and Planetary Sciences*, 38, 439-466.  
952 <https://doi.org/10.1146/annurev-earth-040809-152333>  
953

954 Fletcher, R., Kuznir, N., Roberts, A., Hunsdale, R. 2013. The formation of a failed  
955 continental breakup basin: The Cenozoic development of the Faroe-Shetland Basin. *Basin*  
956 *Research* 25, 532–553.  
957 <https://doi.org/10.1111/bre.12015>  
958

959 Floyd, J.S. Tolstoy, M., Mutter, J.C., Scholz, C.H. 2002. Seismotectonics of Mid-Ocean  
960 Ridge Propagation in Hess Deep. *Science*, 298 (5599), 1765–1768.  
961 <https://doi.org/10.1126/science.1077950>  
962

963 Franke, D., Hinz, K. 2009. Geology of the Shelves surrounding the New Siberian Islands,  
964 Russian Arctic. *Stephan Mueller Special Publication Series* 4, 35-44.  
965 <https://doi.org/10.1029/2003JB002687>  
966

967 Fujita, K., Koz'min, B.M., Mackey, K.G., Riegel, S.A., McLean, M.S., Imaev, V.S. 2009.  
968 Seismotectonics of the Chersky Seismic Belt, eastern Sakha Republic (Yakutia) and  
969 Magadan District, Russia. *Stephen Mueller Special Publication Series* 4, 117-145.  
970 <http://doi.org/10.5194/smsps-4-117-2009>  
971

972 GEBCO 2019. Global Bathymetric map of the Ocean.  
973 <https://www.gebco.net/>  
974

975 Glebovsky, V.Yu., Kaminsky, V.D., Minakov, A.N., Merkur'ev, S.A., Childers, V.A., Brozena,  
976 J. M. 2006. Formation of the Eurasia Basin in the Arctic Ocean as inferred from  
977 geohistorical analysis of the anomalous magnetic field. *Geotectonics* 40, 263-281.  
978 <https://doi.org/10.1134/S0016852106040029>  
979

980 Goodliffe, A.M., Taylor, B. 2007. The boundary between continental rifting and sea-floor  
981 spreading in the Woodlark Basin, Papua New Guinea. Geological Society, London, Special  
982 Publications 282, 217-238.  
983 <https://doi.org/10.1144/SP282.11>  
984

985 Handin, J., 1969. On the Coulomb–Mohr failure criterion. *Journal of Geophysical Research*  
986 74, 5343–5348.  
987 <https://doi.org/10.1029/JB074i022p05343>  
988

989 Hey, R., Martinez, F., Höskuldsson, Á, Benediktsdóttir, Á. 2010. Propagating rift model for  
990 the V - shaped ridges south of Iceland. *Geochemistry, Geophysics, Geosystems* 11,  
991 Q03011.  
992 <https://doi.org/10.1029/2009GC002865>

993  
994 Holm, R.J., Rosenbaum, G., Richards, S.W. 2016. Post 8 Ma reconstruction of Papua New  
995 Guinea and Solomon Islands: Microplate tectonics in a convergent plate boundary setting.  
996 *Earth-Sciences Reviews* 156, 66-81.  
997 <http://dx.doi.org/10.1016/j.earscirev.2016.03.005>  
998  
999 Hubbert, M.K. 1937. Theory of scaled models as applied to the study of geological  
1000 structures. *Geological Society of America Bulletin* 48, 1459-1520.  
1001 <https://doi.org/10.1130/GSAB-48-1459>  
1002  
1003 Huismans, R.S., Podladchikov, Y.Y., Cloething, S. 2001. Transition from passive to active  
1004 rifting- Relative importance of asthenospheric doming and passive extension of the  
1005 lithosphere. *Journal of Geophysical Research* 106, 11,271-11,291.  
1006 <https://doi.org/10.1029/2000JB900424>  
1007  
1008 Imaeva, L.P., Imaev, V.S., Koz'min, B.M. 2016. Structural-dynamic model of the Chersky  
1009 seismotectonic zone (continental part of the Arctic-Asian seismic belt). *Journal of Asian*  
1010 *Earth Sciences* 116, 59-68.  
1011 <https://doi.org/10.1016/j.jseaes.2015.11.010>  
1012  
1013 Jackson, C.A.-L., Bell, R.E., Rotevatn, A., Tverndt, A.B.M. Techniques to determine the  
1014 kinematics of synsedimentary normal faults and implications for fault growth models.  
1015 *Geological Society, London, Special Publications* 439.  
1016 <https://doi.org/10.1144/SP439.22>  
1017  
1018 Jakobsson, M., Mayer, L.A., Coakley, B., Dowdeswell, J.A., Forbes, S., Fridman, H.  
1019 Hodnesdal, B., Noormets, R., Pedersen, R., Rebesco, M., Schenke, H.-W., Zarayskaya  
1020 A.Y., Accettella, D., Armstrong, A., Anderson, R.M., Bienhoff, P., Camerlenghi, A., Church,  
1021 I., Edwards, M., Gardner, J.V., Hall, J.K., Hell, B., Hestvik, O.B., Kristoffersen, Y.,  
1022 Marcussen, C., Mohammad, R., Mosher, D., Nghiem, S.V., Pedrosa, M.T., Travaglini, P.G.,  
1023 Weatherall, P. 2012. The International Bathymetric Chart of the Arctic Ocean (IBCAO)  
1024 Version 3.0, *Geophysical Research Letters* 39, L12609.  
1025 <http://doi.org/10.1029/2012GL052219>  
1026  
1027 Jaeger, J.C., Cook, N.G.W., 1976. *Fundamentals of Rock Mechanics*. Chapman & Hall,  
1028 Wiley, New York.  
1029  
1030 Keep, M., and McClay, K. R., 1997. Analogue modelling of multiphase rift systems,  
1031 *Tectonophysics*, 273, 239-270.  
1032 [https://doi.org/10.1016/S0040-1951\(96\)00272-7](https://doi.org/10.1016/S0040-1951(96)00272-7)  
1033  
1034 Klinkmüller, M., Schreurs, G., Rosenau, M., Kemnitz, H. 2016. Properties of granular  
1035 analogue model materials: A community wide survey. *Tectonophysics* 684, 23-38.  
1036 <http://dx.doi.org/10.1016/j.tecto.2016.01.017>  
1037  
1038 Kydonakis, K, Brun, J.-P., Sokoutis, D. 2015. North Aegean core complexes, the gravity  
1039 spreading of a thrust wedge. *Journal of Geophysical Research: Solid Earth* 120, 595-616.  
1040 <https://doi.org/10.1002/2014JB011601>  
1041

1042 Le Calvez, J.H., Vendeville, B.C. 2002. Experimental designs to model along-strike fault  
1043 interaction. *Journal of the Virtual Explorer* 7, 1-17.  
1044 <https://doi.org/10.3809/jvirtex.2002.00043>  
1045  
1046 Le Pourhiet, L., Chamot-Rooke, N., Delescluse, M., May, D.A., Watremez, L., Pubellier, M.  
1047 2018. Continental break-up of the South China Sea stalled by far-field compression. *Nature*  
1048 *Geoscience* 11, 605-609.  
1049 <https://doi.org/10.1038/s41561-018-0178-5>  
1050  
1051 Ligi, M., Bonatti, E., Bortoluzzi, G., Cipriani, A., Cocchi, L., Caratori Tontini, F., Carmi-  
1052 nati, E., Ottolini, L., Schettino, A., 2012. Birth of an ocean in the Red Sea: initial pangs.  
1053 *Geochemistry, Geophysics, Geosystems* 13, Q08009.  
1054 <http://dx.doi.org/10.1029/2012GC004155>  
  
1055 Little, T.A., Baldwin, S.L., Fitzgerald, P.G., Monteleone, B. 2007. Continental rifting and  
1056 metamorphic core complex formation ahead of the Woodlark spreading ridge,  
1057 D'Entrecasteaux Islands, Papua New Guinea. *Tectonics* 26, TC1002.  
1058 <https://doi.org/10.1029/2005TC001911>  
1059  
1060 Manighetti, I., Taponnier, P., Courtillot, V., Gruszow, S., Gillot, P.-Y. 1997. Propagation of  
1061 rifting along the Arabia-Somalia Plate Boundary: The Gulfs of Aden and Tadjoura. *Journal*  
1062 *of Geophysical Research* 102, 2681-2710.  
1063 <https://doi.org/10.1029/96JB01185>  
1064  
1065 Mart, Y., Dauteuil, O. 2000. Analogue experiments of propagation of oblique rifts.  
1066 *Tectonophysics* 316, 121-132.  
1067 [https://doi.org/10.1016/S0040-1951\(99\)00231-0](https://doi.org/10.1016/S0040-1951(99)00231-0)  
1068  
1069 Martin, A.K. 1984. Propagating rifts: Crustal extension during continental rifting. *Tectonics*  
1070 3, 611-617.  
1071 <https://doi.org/10.1029/TC003i006p00611>  
1072  
1073 McClusky, S., Reilinger, R., Ogubazghi, G., Amleson, A., Healeb, B., Vernant, P., Sholan,  
1074 J., Fisseha, S., Asfaw, L., Bendick, R., Kogan, L. 2010. Kinematics of the southern Red  
1075 Sea-Afar Triple Junction and implications for plate dynamics. *Geophysical Research*  
1076 *Letters* 37, L05301.  
1077 <https://doi.org/10.1029/2009GL041127>  
1078  
1079 McKenzie, D.P. 1978. Some remarks on the development of sedimentary basins. *Earth and*  
1080 *Planetary Science Letters* 40, 25-32.  
1081 [https://doi.org/10.1016/0012-821X\(78\)90071-7](https://doi.org/10.1016/0012-821X(78)90071-7)  
1082  
1083 McKenzie, D., Nimmo, F., Jackson, J.A. 2000. Characteristics and consequences of flow in  
1084 the lower crust. *Journal of Geophysical Research* 105, B5, 11029-11046.  
1085 <https://doi.org/10.1029/1999JB900446>  
1086  
1087 Meschede, M., Barckhausen, U. 2000. Meschede, M., and Barckhausen, U., 2000. Plate  
1088 tectonic evolution of the Cocos-Nazca spreading center. In Silver, E.A., Kimura, G., and  
1089 Shipley, T.H. (Eds.), *Proceedings of the Ocean Drilling Program, Scientific Results 170*.  
1090 College Station, TX

1091 [http://www-odp.tamu.edu/publications/170\\_SR/chap\\_07/chap\\_07.htm](http://www-odp.tamu.edu/publications/170_SR/chap_07/chap_07.htm)  
1092  
1093 Michon, L., Merle, O. 2000. Crustal structures of the Rhinegraben and the Massif Central  
1094 grabens: An experimental approach. *Tectonics* 19 (5), 896-904.  
1095 <https://doi.org/10.1029/2000TC900015>  
1096  
1097 Molnar, N.E., Cruden, A.R., Betts, P.G. 2017. Interactions between propagating rotational  
1098 rifts and linear rheological heterogeneities: Insights from three-dimensional laboratory  
1099 experiments. *Tectonics* 36, 420-443.  
1100 <https://doi.org/10.1002/2016TC004447>  
1101  
1102 Molnar, N.E., Cruden, A.R., Betts, P.G. 2018. Unzippingg continents and the birth of  
1103 microcontinents. *Geology* 46, 451–454  
1104 <https://doi.org/10.1130/G40021.1>  
1105  
1106 Molnar, N.E., Crusden, A. R., Betts, P.G. Interactions between propagating rifts and linear  
1107 weaknesses in the lower crust. *Geosphere* 15, 1617-1640.  
1108 <https://doi.org/10.1130/GES02119.1>  
1109  
1110 Mondy, L.S., Patrice, F.R., Duclaux, G., Mores, L. 2018. The role of asthenospheric flow  
1111 during rift propagation and breakup. *Geology* 46, 103-106.  
1112 <https://doi.org/10.1130/G39674.1>  
1113  
1114 Morley, C. K., 1999, How successful are analogue models in addressing the influence of  
1115 pre-existing fabrics on rift structure?: *Journal of Structural Geology*, 21, 1267– 1274.  
1116 [https://doi.org/10.1016/S0191-8141\(99\)00075-9](https://doi.org/10.1016/S0191-8141(99)00075-9)  
1117  
1118 Moucha, R., Forte, A.E., 2008. Changes in African topography driven by mantle convection.  
1119 *Nature Geoscience* 4, 707-712.  
1120 <https://doi.org/10.1038/NGEO1235>  
1121  
1122 Mulugeta, G. 1988. Squeeze box in the centrifuge. *Tectonophysics* 148, 323-335.  
1123 [https://doi.org/10.1016/0040-1951\(88\)90139-4](https://doi.org/10.1016/0040-1951(88)90139-4)  
1124  
1125 Murton, B.J., Rona, P.A. 2015. Carlsberg Ridge and Mid-Atlantic Ridge: Comparison of  
1126 slow spreading centre analogues. *Deep Sea Research Part II: Topical Studies in*  
1127 *Oceanography* 121, 71-84.  
1128 <https://doi.org/10.1016/j.dsr2.2015.04.021>  
1129  
1130 Naliboff, J., Buiter, S.J.H. 2015. Rift reactivation and migration during multiphase extension.  
1131 *Earth and Planetary Science Letters* 421, 58–67.  
1132 <http://dx.doi.org/10.1016/j.epsl.2015.03.050>  
1133  
1134 Panien, M., Schreurs, G, Pfiffner, A. 2006. Mechanical behaviour of granular materials used  
1135 in analogue modelling: insights from grain characterisation, ring-shear tests and analogue  
1136 experiments. *Journal of Structural Geology* 28, 1710-1724.  
1137 <https://doi.org/10.1016/j.jsg.2006.05.004>  
1138  
1139 Péron-Pinvidic, G., Manatschal, G. 2010. From microcontinents to extensional allochthons:  
1140 witnesses of how continents rift and break apart? *Petroleum Geoscience* 16, 189-197.

1141 <https://doi.org/10.1144/1354-079309-903>  
1142  
1143 Philippon, M., Willingshofer, E., Sokoutis, D., Corti, G., Sani, F., Bonini, M., Cloetingh, S.  
1144 2015. Slip re-orientation in oblique rifts. *Geology* 43, 147-150.  
1145 <https://doi.org/10.1130/G36208.1>  
1146  
1147 Prada, M., Watremez, L., Chen, C., O'Reilly, B., Minshull, T., Reston, T., Shannon, P.,  
1148 Klaeschen, D., Wagner, G., Gaw, V., 2017. Crustal strain-dependent serpentinisation in the  
1149 Porcupine Basin, offshore Ireland' *Earth and Planetary Science Letters*, vol. 474, pp. 148-  
1150 159.  
1151 <https://doi.org/10.1016/j.epsl.2017.06.040>  
1152  
1153 Ramberg, H. 1981. *Gravity, Deformation and the Earth's Crust*. Academic Press, London.  
1154  
1155 Rotevatn, A., Jackson, C.A.-L., Tvedt, A.B.M., Bell, R.E., Blækkan, I. How do normal faults  
1156 grow? *Journal of Structural Geology*.  
1157 <https://doi.org/10.1016/j.jsg.2018.08.005>  
1158  
1159 Rudolf, M., Boutelier, D., Rosenau, M., Schreurs, G., Oncken, O., 2016. Rheological  
1160 benchmark of silicone oils used for analog modeling of short- and long-term lithospheric  
1161 deformation, *Tectonophysics* 684, 12-22. <http://dx.doi.org/10.1016/j.tecto.2015.11.028>  
1162  
1163 Saria, E., Calais, E., Stamps, D.S., Delvaux, D., Hartnady, C.J.H. 2014. Present-day  
1164 kinematics of the East African Rift. *Journal of Geophysical Research. Solid Earth* 119,  
1165 3584-3600.  
1166 <https://doi.org/10.1002/2013JB010901>  
1167  
1168 Savva, D., Pubelier, M., Franke, D., Chamot-Rooke, N., Meresse, F., Steuer, S., Auxietre,  
1169 J.L. 2014. Different expressions of rifting on the South China Sea margins. *Marine and*  
1170 *Petroleum Geology* 58, part B, 579-598.  
1171 <http://dx.doi.org/10.1016/j.marpetgeo.2014.05.023>  
1172  
1173 Schellart, W.P., Lister, G.S., Jessell, M.W. 2002. Analogue modelling of asymmetrical back-  
1174 arc extension. In: Schellart, W.P., Passchier, C. (eds.) *Analogue modelling of large-scale*  
1175 *tectonic processes*. *Journal of the Virtual Explorer* 7, 25-42.  
1176 <https://doi.org/10.3809/jvirtex.2002.00046>  
1177  
1178 Schellart, W.P., Jessell, M.W., Lister, G.S. 2003. Asymmetric deformation in the backarc  
1179 region of the Kuril arc, northwest Pacific: New insights from analogue modelling. *Tectonics*  
1180 22, 1047.  
1181 <https://doi.org/10.1029/2002TC001473>  
1182  
1183 Schlagenhauf, A., Manighetti, I., Malavieille, J., Dominguez, S., 2008. Incremental growth of  
1184 normal faults: Insights from a laser-equipped analog experiment. *Earth and Planetary*  
1185 *Science Letters* 273, 299–311  
1186 <https://doi.org/10.1016/j.epsl.2008.06.042>  
1187  
1188 Schultz, R.A. 1993. Brittle strength of basaltic rock masses with applications to Venus.  
1189 *Journal of Geophysical Research* 98, 10,883-10,895.  
1190 <https://doi.org/10.1029/93JE00691>

1191  
1192 Seebeck, H., Nicol, A., Villamor, P., Ristau, J., Pettinga, J. 2014. Structure and kinematics  
1193 of the Taupo Rift, New Zealand. *Tectonics* 33, 1178-1199.  
1194 <https://doi.org/10.1002/2014TC003569>  
1195  
1196 Shinevar, W.J., Behn, M.D., Hirt, G., 2015. Compositional dependence of lower crustal  
1197 viscosity. *Geophysical Research Letters* 42, 8333–8340.  
1198 <https://doi.org/10.1002/2015GL065459>  
1199  
1200 Smith, J.V. 1993. Infinitesimal kinematics of rotational rifting with reference to en echelon  
1201 marginal faults in the Red Sea region. *Tectonophysics* 222, 227-235.  
1202 [https://doi.org/10.1016/0040-1951\(93\)90050-T](https://doi.org/10.1016/0040-1951(93)90050-T)  
1203  
1204 Souriot, T., Brun, J.-P. 1992. Faulting and block rotation in the Afar triangle, East Africa:  
1205 The Danakil “crank-arm” model. *Geology* 20, 911-914.  
1206 [https://doi.org/10.1130/0091-7613\(1992\)020<0911:FABRIT>2.3.CO;2](https://doi.org/10.1130/0091-7613(1992)020<0911:FABRIT>2.3.CO;2)  
1207  
1208 Stab, M., Bellahsen, N., Quicelleur, X., Ayalew, D., Leroy, S., 2016. Modes of rifting in  
1209 magma-rich settings: Tectonomagmatic evolution of Central Afar. *Tectonics*, 35, 2-38.  
1210 <https://doi.org/10.1002/2015TC003893>  
1211  
1212 Sun., Z., Zhong, Z., Keep, M., Zhou, D., Cai, D., Li, X., Wu, S., Jiang, J. 2009. 3D analogue  
1213 modelling of the South China Sea: A discussion on breakup pattern. *Journal of Asian Earth*  
1214 *Sciences* 34, 544-556.  
1215 <https://doi.org/10.1016/j.jseaes.2008.09.002>  
1216  
1217 Tate, M.P. 1993. Structural framework and tectono-stratigraphic evolution of the Porcupine  
1218 Seabight Basin, offshore Western Ireland. *Marine and Petroleum Geology*, 10(2), 95–123.  
1219 [https://doi.org/10.1016/0264-8172\(93\)90016-L](https://doi.org/10.1016/0264-8172(93)90016-L)  
1220  
1221 Taylor, B., Goodliffe, A., Martinez, F., Hey, R. 1995. Continental rifting and initial sea-floor  
1222 spreading in the Woodlark basin. *Nature*, 374 (6522), 534–537.  
1223 <https://doi.org/10.1038/374534a0>  
1224  
1225 Taylor, B., Goodliffe, A.M., Martinez, F., 1999. How continents break up: insights from  
1226 Papua New Guinea. *Journal of Geophysical Research, Solid Earth* 104, 7497–7512.  
1227 <https://doi.org/10.1029/1998JB900115>  
1228  
1229 Tron, V. Brun, J.-P. 1991, Experiments on oblique rifting in brittle-ductile systems.  
1230 *Tectonophysics* 188, 71-88.  
1231 [https://doi.org/10.1016/0040-1951\(91\)90315-J](https://doi.org/10.1016/0040-1951(91)90315-J)  
1232  
1233 Twiss, R.J., Moores, E.M., 2007. *Structural Geology*, 2<sup>nd</sup> edition. W.H. Freeman and  
1234 Company, New York  
1235  
1236 Van der Pluijm, B.A., Marshak, S. 2004. *Earth Structure*, 2<sup>nd</sup> edition. W.W. Norton &  
1237 Company Ltd., New York.  
1238  
1239 Underhill, J.R., Partington, M.A. 1993. Jurassic thermal doming and deflation in the North  
1240 Sea: implications of the sequence stratigraphic evidence. In: Parker, J.R. (ed) *Petroleum*

1241 Geology: North-West Europe and Global Perspectives - Proceedings of the 4th Petroleum  
1242 Geology Conference. Geological Society Petroleum Geology Conference Series 4, 337–  
1243 345.  
1244 <https://doi.org/10.1144/0040337>  
1245  
1246 Van Wijk, J.W., Blackman, D.K. 2005. Dynamics of continental rift propagation: the end-  
1247 member modes. Earth and Planetary Science Letters 229, 247-258.  
1248 <https://doi.org/10.1016/j.epsl.2004.10.039>  
1249  
1250 Vink, G.E. 1982. Continental rifting and the implications for plate tectonic reconstructions.  
1251 Journal of Geophysical Research 87, 10,667-10,688.  
1252 <https://doi.org/10.1029/JB087iB13p10677>  
1253  
1254 Wallace, L.M., Beavan, J., McCaffrey, R., Darby, D. 2004. Subduction zone coupling and  
1255 tectonic block rotations in the North Island, New Zealand. Journal of Geophysical Research  
1256 109, B12406.  
1257 <https://doi.org/10.1029/2004JB003241>  
1258  
1259 Wallace, L.M., Ellis, S., Mann, P. 2009. Collisional model for rapid fore-arc block rotations,  
1260 arc curvature, and episodic back-arc rifting in subduction settings. Geochemistry,  
1261 Geophysics, Geosystems 10, Q05001.  
1262 <https://doi.org/10.1029/2008GC002220>  
1263  
1264 Weijermars, R., Schmeling, H. 1986. Scaling of Newtonian and non-Newtonian fluid  
1265 dynamics without inertia for quantitative modelling of rock flow due to gravity (including the  
1266 concept of rheological similarity). Physics of Earth and Planetary Interiors 43, 316-330.  
1267 [https://doi.org/10.1016/0031-9201\(86\)90021-X](https://doi.org/10.1016/0031-9201(86)90021-X)  
1268  
1269 Weissel, J.K., Watts, A.B., 1979. Tectonic evolution of the Coral Sea Basin. Journal of  
1270 Geophysical Research 84, 4572-4582.  
1271 <https://doi.org/10.1029/JB084iB09p04572>  
1272  
1273 Wernicke, B. 1985. Uniform-sense normal simple shear of the continental lithosphere  
1274 Canadian Journal of Earth Sciences 22, 108-125,  
1275 <https://doi.org/10.1139/e85-009>  
1276  
1277 Withjack, M.O., Jamison, W.R. 1986. Deformation produced by oblique rifting.  
1278 Tectonophysics 126, 99-124.  
1279 [https://doi.org/10.1016/0040-1951\(86\)90222-2](https://doi.org/10.1016/0040-1951(86)90222-2)  
1280  
1281 Wolfenden, E., Ebinger, C., Yirgu, G., Deino, A., Ayalew, D., 2004. Evolution of the northern  
1282 Main Ethiopian rift: birth of a triple junction. Earth and Planetary Science Letters 224, 213-  
1283 228.  
1284 <https://doi.org/10.1016/j.epsl.2004.04.022>  
1285  
1286 Zhou, D., Ru, K., Chen, H.-z. 1995. Kinematics of Cenozoic extension on the South China  
1287 Sea continental margin and its implications for the tectonic evolution of the region.  
1288 Tectonophysics 251, 161-177.  
1289 [https://doi.org/10.1016/0040-1951\(95\)00018-6](https://doi.org/10.1016/0040-1951(95)00018-6)  
1290

1291 Zwaan, F., G. Schreurs, J. Naliboff, Buitter, S.J.H. 2016. Insights into the effects of oblique  
1292 extension on continental rift interaction from 3D analogue and numerical models.  
1293 Tectonophysics 693, 239-260.  
1294 <https://doi.org/10.1016/j.tecto.2016.02.036>  
1295

1296 Zwaan, F., Schreurs, G. Adam, J., 2018a. Effects of sedimentation on rift segment evolution  
1297 and rift interaction in orthogonal and oblique extensional settings: Insights from analogue  
1298 models analysed with 4D X-ray computed tomography and digital volume correlation  
1299 techniques. Global and Planetary Change 171, 110-133.  
1300 <https://doi.org/10.1016/j.gloplacha.2017.11.002>  
1301

1302 Zwaan, F., Schreurs, G., Gentzmann, R., Warsitzka, M. & Rosenau, M. (2018b). Ring-shear  
1303 test data of quartz sand from the Tectonic Modelling Lab of the University of Bern (CH). V.  
1304 1. GFZ Data Services.  
1305 <http://doi.org/10.5880/fidgeo.2018.028>  
1306

1307 Zwaan, F., Schreurs, G., Ritter, M., Santimano, T. & Rosenau, M. (2018c). Rheology of  
1308 PDMS-corundum sand mixtures from the Tectonic Modelling Lab of the University of Bern  
1309 (CH). V. 1. GFZ Data Services  
1310 <http://doi.org/10.5880/fidgeo.2018.023>  
1311  
1312

1313 Zwaan, F., Schreurs, G., Buitter, S.J.H. (2019). A systematic comparison of experimental  
1314 set-ups for modelling extensional tectonics. Solid Earth 10, 1063-1097.  
1315 <https://doi.org/10.5194/se-10-1063-2019>  
1316

1317 Zwaan, F., Schreurs, G., Schmid, T., Warsitzka, M. & Rosenau, M. (2020). Digital image  
1318 correlation data from analogue modelling experiments addressing orthogonal and rotational  
1319 extension at the Tectonic Modelling Lab of the University of Bern (CH), GFZ Data Services.  
1320 <http://doi.org/10.5880/FIDGEO.2020.001>  
1321 **NB: Temporary link (Data Publication is not officially finalized):**  
1322 [http://pmd.gfz-  
potsdam.de/panmetaworks/review/727b14a07cbea4b20911d443b6586d822f9270554c78f6  
6186d107ffb2bf20d0](http://pmd.gfz-<br/>1323 potsdam.de/panmetaworks/review/727b14a07cbea4b20911d443b6586d822f9270554c78f6<br/>1324 6186d107ffb2bf20d0)

1325  
1326  
1327  
1328

## Tables

Table 1. Material properties

Granular materials	Quartz sand <sup>a</sup>	Corundum sand <sup>b</sup>
Grain size range ( $\phi$ )	60-250 $\mu\text{m}$	88-125 $\mu\text{m}$
Specific density <sup>c</sup> ( $\rho_{\text{specific}}$ )	2650 $\text{kg/m}^3$	3950 $\text{kg/m}^3$
Sieved density ( $\rho_{\text{sieved}}$ )	1560 $\text{kg/m}^3$	1890 $\text{kg/m}^3$
Angle of internal peak friction	36.1°	37°
Angle of dynamic-stable friction	31.4°	32°
Cohesion	9 $\pm$ 98 Pa	39 $\pm$ 10 Pa
Viscous materials	Pure PDMS <sup>d</sup>	PDMS/corundum sand mixture <sup>a</sup>
Weight ratio PDMS : corundum sand	-	0.965 kg : 1.00 kg
Density ( $\rho$ )	965 $\text{kg/m}^3$	ca. 1600 $\text{kg/m}^3$
Viscosity ( $\eta$ )	ca. $2.5 \cdot 10^4$ Pa·s	ca. $1.5 \cdot 10^5$ Pa·s <sup>e</sup>
Type <sup>f</sup>	Newtonian (n = ca. 1)	near-Newtonian (n = 1.05-1.10)

1329  
1330  
1331  
1332  
1333  
1334  
1335  
1336  
1337  
1338  
1339  
1340

<sup>a</sup> Quartz sand, PDMS and viscous mixture characteristics after Zwaan et al. (2016; 2018b, c)

<sup>b</sup> Corundum sand characteristics after Panien et al. (2006)

<sup>c</sup> Specific densities after Carlo AG (2019)

<sup>d</sup> Pure PDMS rheology after Rudolf et al. (2016)

<sup>e</sup> Viscosity value holds for model strain rates  $< 10^{-4} \text{ s}^{-1}$

<sup>f</sup> Power-law exponent n (dimensionless) represents sensitivity to strain rate

Table 2. Model characteristics

Series	Model	Seed length (L)	CT- scanned	Shown in
Orthogonal extension (O)	O1	-	-	Figs. 4-6, C1
	O2	-	-	Fig. B1
	O3	Full (80cm)	x	Figs. 4-7, 9, B1, C1
Rotational extension (R)	R1	-	-	Figs. 4-6, C1
	R2	Full (65+25 cm)	-	Fig. B1
	R3	Full (65+25 cm)	x	Figs. 4-6, 8, 9, B1, C1

1341  
1342  
1343

1344 Table 3. Scaling parameters  
 1345  
 1346  
 1347  
 1348  
 1349

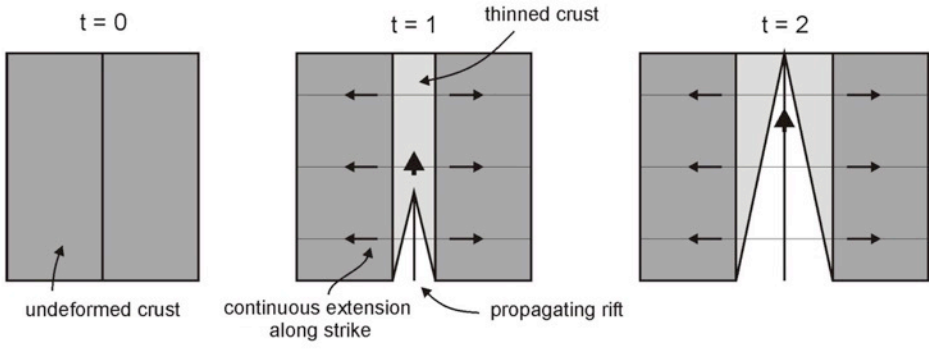
		<b>Model</b>	<b>Nature (continent)</b>	<b>Nature (ocean)</b>
<b>General parameters</b>	Gravitational accel. (g)	9.81 m/s <sup>2</sup>	9.81 m/s <sup>2</sup>	9.81 m/s <sup>2</sup>
	Extension velocity (v)	2.2·10 <sup>-6</sup> m/s	1.5·10 <sup>-10</sup> m/s	3.6·10 <sup>-10</sup> m/s
<b>Brittle layer</b>	Material/represents	Sand layer	Upper crust	Oceanic crust
	Thickness (h)	4·10 <sup>-2</sup>	2·10 <sup>4</sup>	7·10 <sup>3</sup>
	Density (ρ)	1560 kg/m <sup>3</sup>	2800 kg/m <sup>3</sup>	3000 kg/m <sup>3</sup>
	Cohesion (C)	9 Pa	8·10 <sup>6</sup> Pa	3·10 <sup>6</sup> Pa
<b>Viscous/ ductile layer</b>	Material/represents	PDMS/cor. sand mix	Lower crust	Lithosph. mantle
	Thickness (h)	4·10 <sup>-2</sup> m	2·10 <sup>4</sup> m	4·10 <sup>-2</sup> m
	Density (ρ)	1600 kg/m <sup>3</sup>	2870 kg/m <sup>3</sup>	3075 kg/m <sup>3</sup>
	Viscosity (η)	1.5·10 <sup>5</sup> Pa·s	1·10 <sup>21</sup> Pa·s	5·10 <sup>19</sup> Pa·s
<b>Dynamic scaling values</b>	Brittle stress ratio (R <sub>s</sub> )	68	68	69
	Ramberg number (R <sub>m</sub> )	75	75	81

1350  
 1351

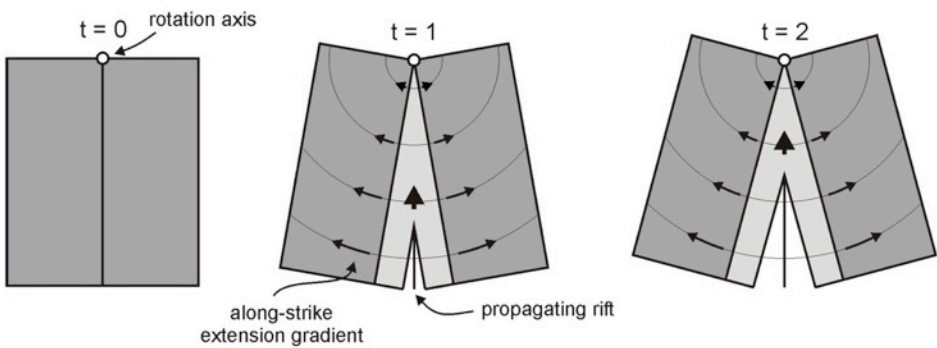
1352  
1353

## Figures and captions

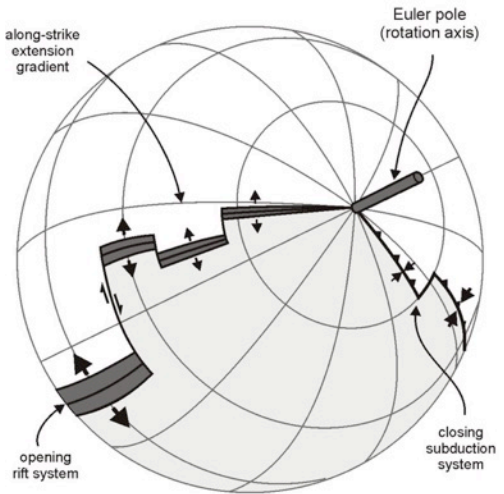
### a) Rift propagation in an orthogonal extension setting



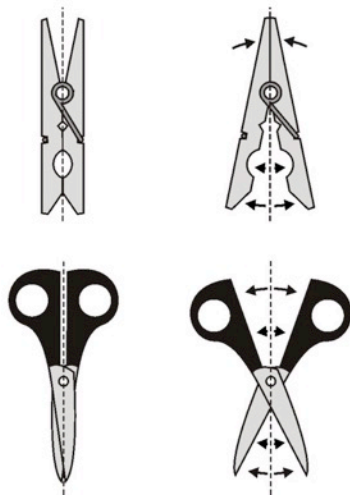
### b) Rift propagation in a rotational extension setting



### c) Opening of a rift system on a sphere

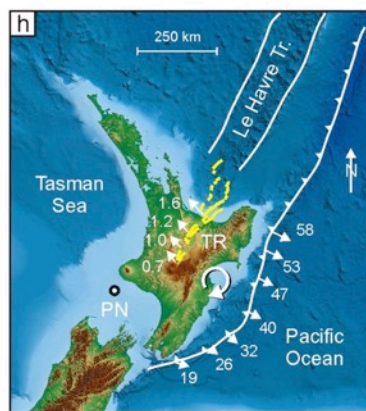
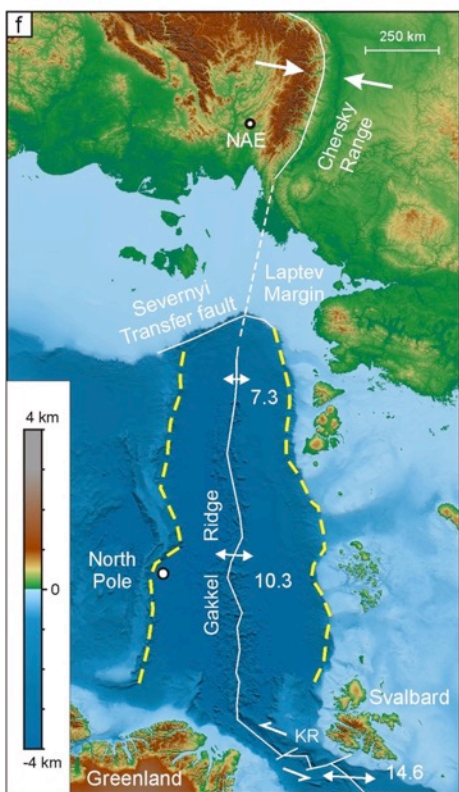
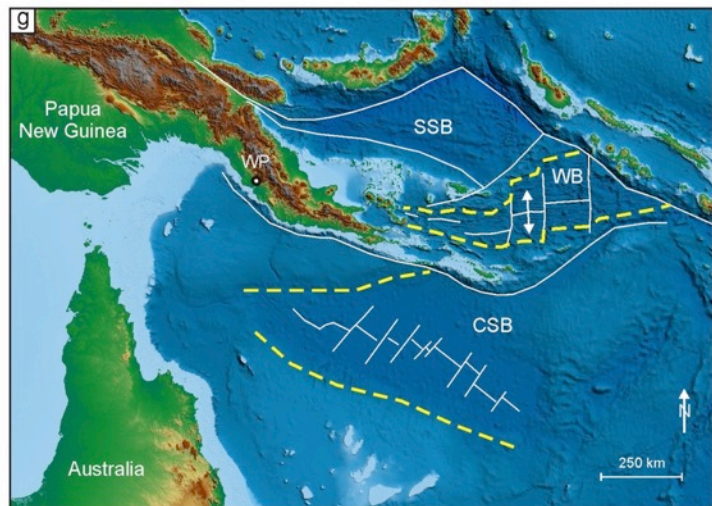
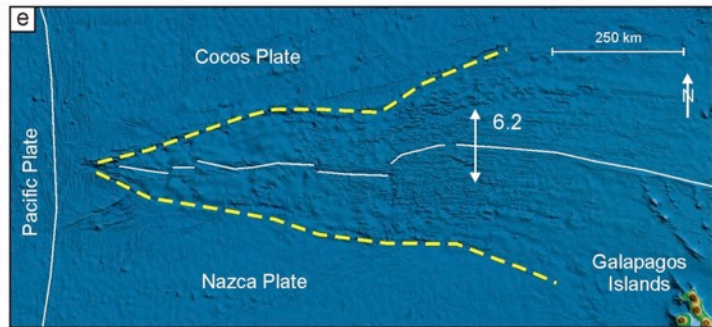
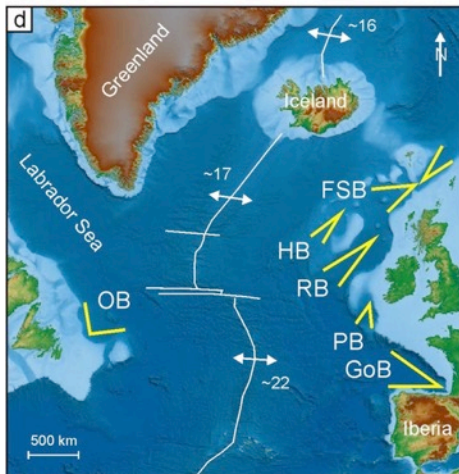
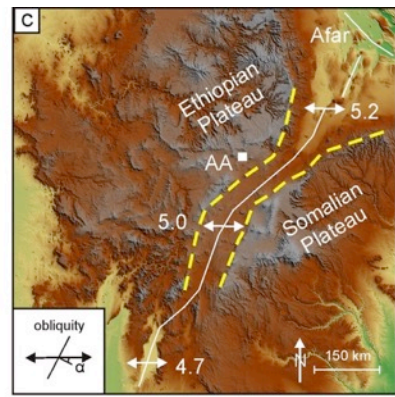
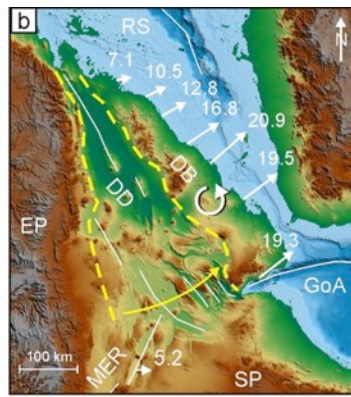
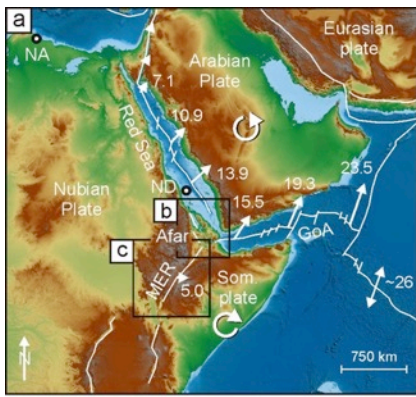


### d) Laundry-peg motion versus scissor motion



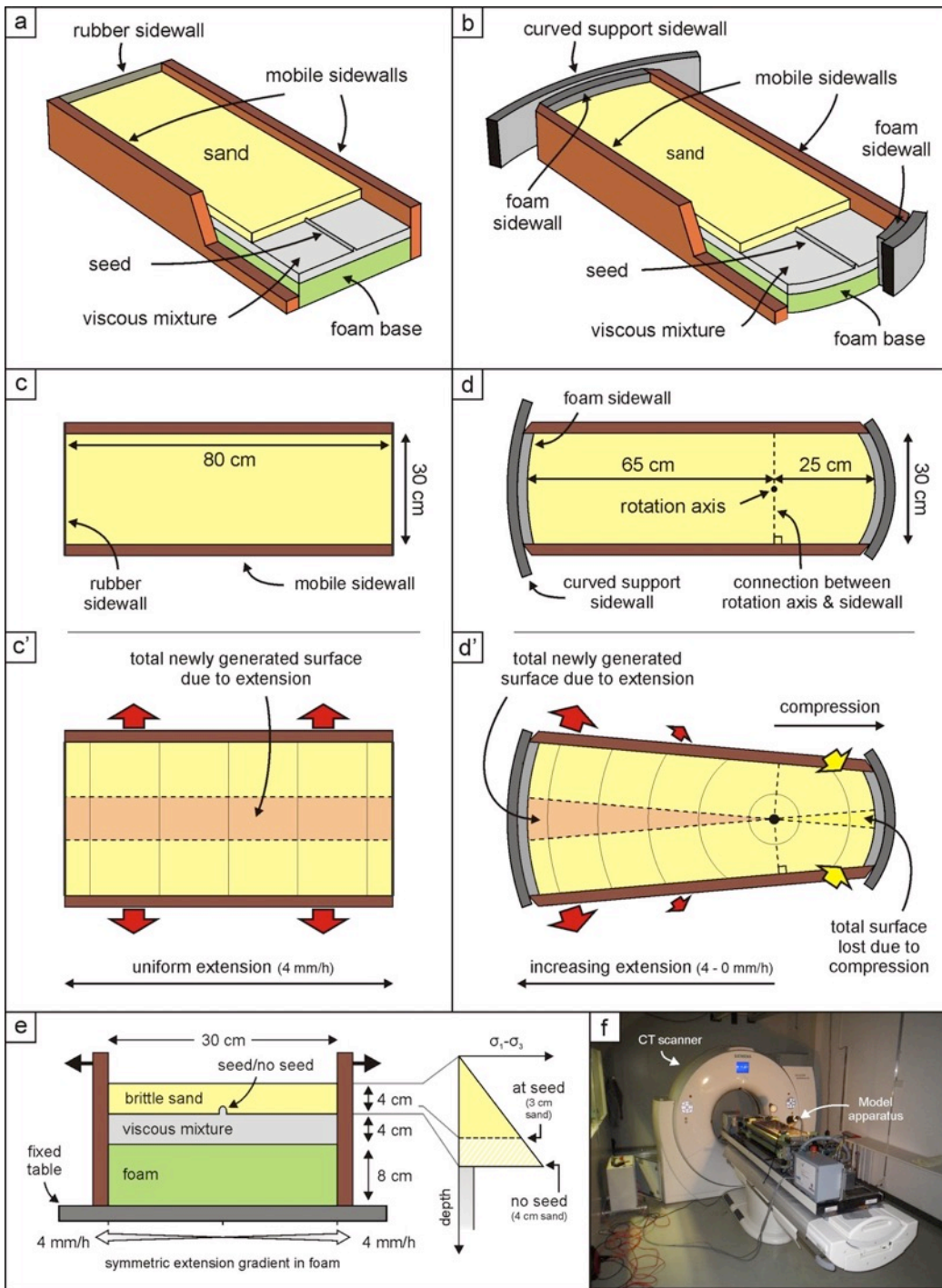
1354  
1355  
1356  
1357  
1358  
1359  
1360  
1361  
1362

Fig. 1. Differences between rift propagation concepts in which (a) extension is continuous along-strike or in which (b) along-strike gradients and a rotation axis are involved, for instance as a result of (c) the opening of a rift system on a global scale. (d) Problems with the term “scissor tectonics”. Top: rotational tectonic motion as seen in nature can be described by the simultaneous opening and closing on opposite sides of the rotation axis (see Figs. 1c, 2e), similar to a laundry peg. Bottom: scissor (tectonic) motion, involving simultaneous extension on both sides of the rotation axis. Image modified after Vink (1982), Martin (1984) and Van der Pluijm & Marshak (2004).



1363  
1364  
1365  
1366

1367 Fig. 2. Examples of extension gradients and V-shaped basins around the world. White lines indicate  
1368 important rift axes or plate boundaries. Yellow (dotted) lines show the borders of the extensional  
1369 systems. When available, GPS-derived extension directions and velocities (in mm/yr), as well as  
1370 rotation axes are indicated. Background topography and bathymetry after the GEBCO (2019) and  
1371 the IBCAO maps (Jacobsson et al. 2012). Note that scale is approximate and may change with  
1372 latitude due to the Mercator projection used for these maps. (a) Extension rate gradients in the Red  
1373 Sea and the Gulf of Aden due to the counterclockwise motion of the Arabian plate about the Nubia-  
1374 Arabian rotation axis (NA). GoA: Gulf of Aden, MER: Main Ethiopian Rift. Image modified after  
1375 Bellahsen et al. (2003), ArRajehi et al. (2010), McClusky et al. (2010), Saria et al. (2014) and  
1376 Murton & Rona (2015). (b) Counterclockwise rotation of the Danakil Block (DB) away from the  
1377 Nubian Plate in Afar, around an axis situated to the north (ND in Fig. 2a). DD: Danakil depression,  
1378 EP: Ethiopian Plateau, GoA: Gulf of Aden, MER: Main Ethiopian Rift, RS: Red Sea, SP: Somalian  
1379 Plateau. For location, see Fig. 2a. Image modified after McClusky et al. 2010 and Saria et al.  
1380 (2014). (c) Continental Main Ethiopian Rift. Image modified after Corti (2009) and Saria et al (2014).  
1381 Inset shows the definition of the degree of extension obliquity as the angle  $\alpha$  between the normal to  
1382 the rift trend and the regional extension direction. AA: Addis Ababa. For location, see Fig. 2a. (d) V-  
1383 shaped basins along the continental margins of the North Atlantic. FSB: Faroe-Shetland Basin,  
1384 GoB: Gulf of Biscay, HB: Hatton Basin, OB: Orphan Basin, PB: Porcupine Basin, RB: Rockall Basin.  
1385 Image modified after DeMets et al. (2010) and Péron-Pinvidic & Manatschal (2010). (e) Oceanic  
1386 Galapagos Ridge in the Pacific. Image modified after Meschede & Barckhausen (2000) and Mondy  
1387 et al. (2018). (g) Current and ancient rift propagation of the oceanic Woodlark and Coral Sea basins  
1388 (WB and CSB, respectively) into continental Papua New Guinea and Australia. SSB: Solomon Sea  
1389 Basin, WP: Woodlark rotation pole. Image modified after Taylor et al. (1999), Goodliffe & Taylor  
1390 2007 and Bulois et al. (2018a). (f) Extension rate gradient along the Arctic Gakkel ridge and  
1391 compression at the Siberian Chersky Range, suggesting plate rotation about a North America-  
1392 Eurasia rotation axis (NAE). KR: Knipovitch Ridge. Image modified after Dick et al. (2003),  
1393 Glebovsky et al. (2006), Fujita et al. (2009) and Imaeva et al. (2016). (h) Taupo Rift (TR) at the tip of  
1394 the Le Havre Trough propagating into New Zealand's Northern Island as a result of rotation of the  
1395 latter with respect to the Pacific plate (PN rotation axis). Image modified after Wallace et al. (2004,  
1396 2009) and Seebeck et al. (2014). (i) V-shape of the South China sub basin (SCSB). Image modified  
1397 after Ding & Li 2016.  
1398  
1399  
1400  
1401



1402  
 1403  
 1404 Fig. 3. Model set-ups. (a) 3D set-up for orthogonal extensional models. (b) 3D set-up for rotational  
 1405 extensional models. (c-c') Top view sketch depicting orthogonal extension deformation. (d-d') Top  
 1406 view sketch illustrating rotational tectonic deformation. The sidewalls are fixed to the rotation axis  
 1407 via a connection at the base of the apparatus (dotted line) in order to produce extension or  
 1408 shortening on either side of the model. Note that in both (c') and (d') extension is exaggerated to  
 1409 highlight the differences between both set-up (compare with Fig. 1a, b) (e) Left: schematic section  
 1410 through the extensional domain of our models, depicting the brittle-viscous layering, seed, the foam  
 1411 base and the extension gradient developing when the sidewalls move apart, as well as the fixed  
 1412 table on which the foam itself rests. Right: schematic strength profile, depicting the difference in  
 1413 brittle strength at and away from the seed. In the former case, the brittle strength (profile surface) is  
 1414 56% weaker due to a brittle layer thickness reduction of 25% (Appendix A1). (f) Model run in the CT  
 1415 scanner.

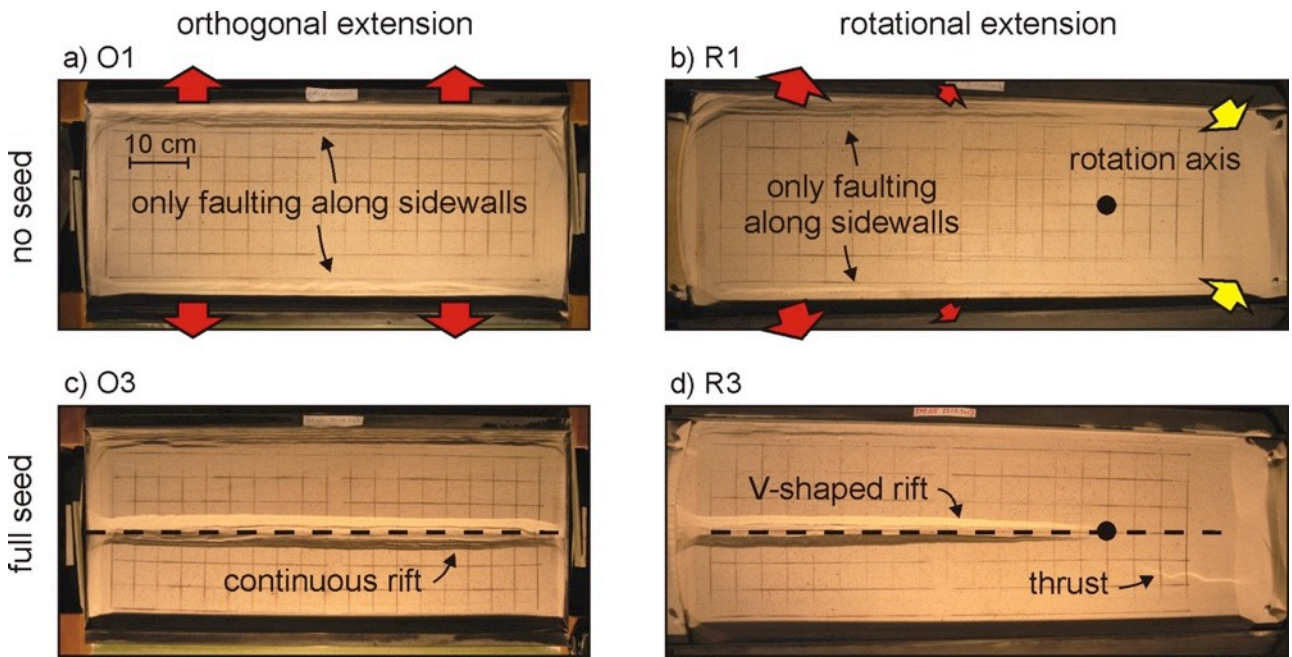


Fig. 4. Overview of final surface structures depicted in map view. Dotted lines indicate the seed trace.

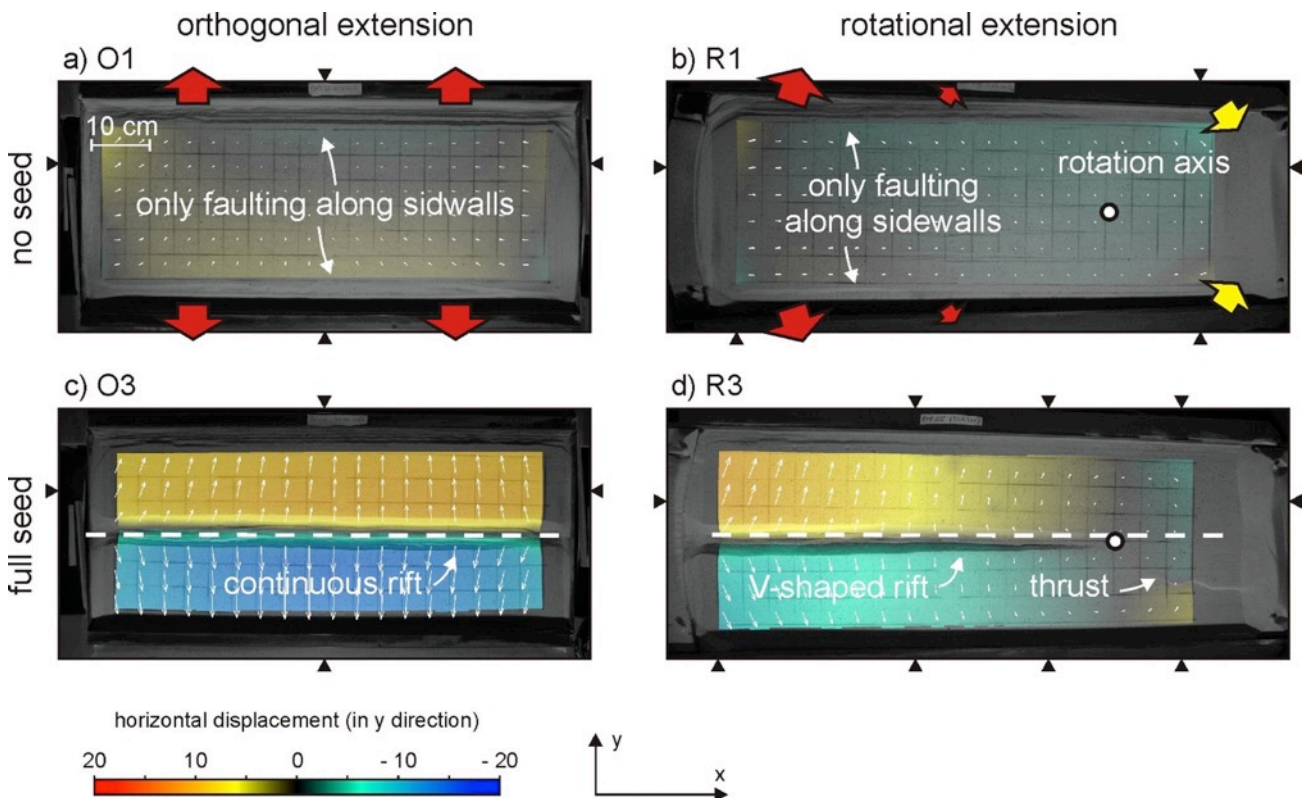


Fig. 5. Overview of DIC analysis results in map view. White arrows indicate total cumulative horizontal displacement, whereas colors display across-strike displacement (i.e. in y-direction) after 40 mm of extension. Dotted lines indicate the seed trace. Triangles along the image margins indicate the locations of profiles along which deformation is plotted in Fig. 6.

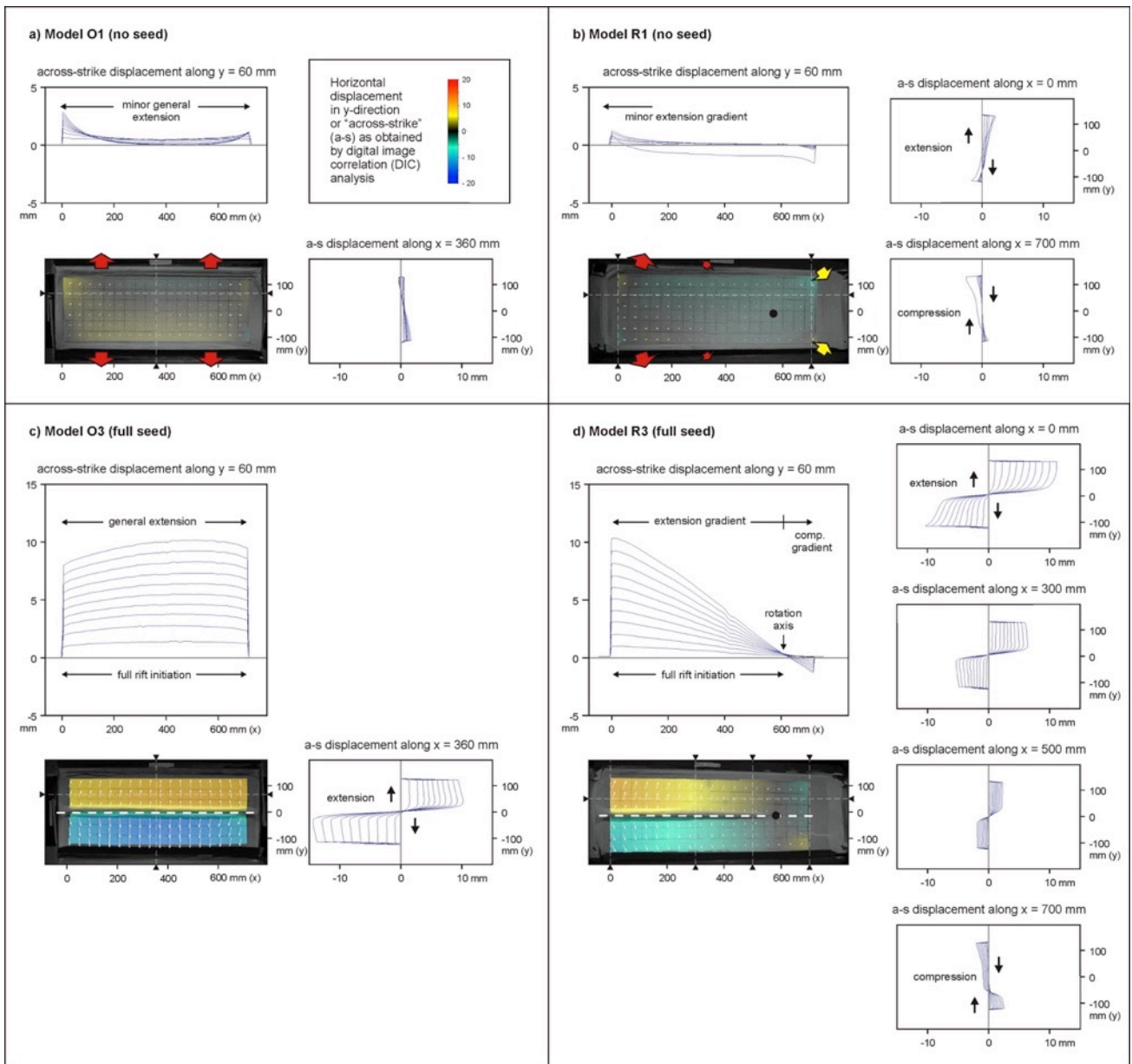
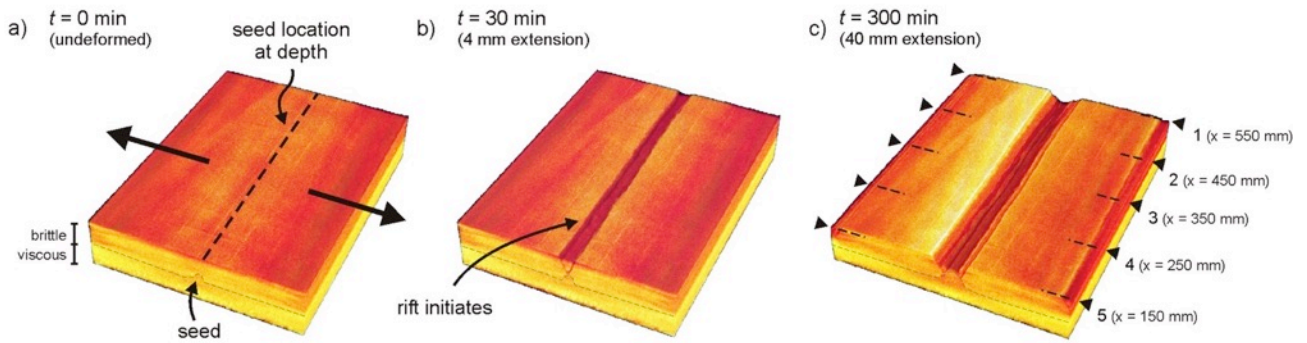


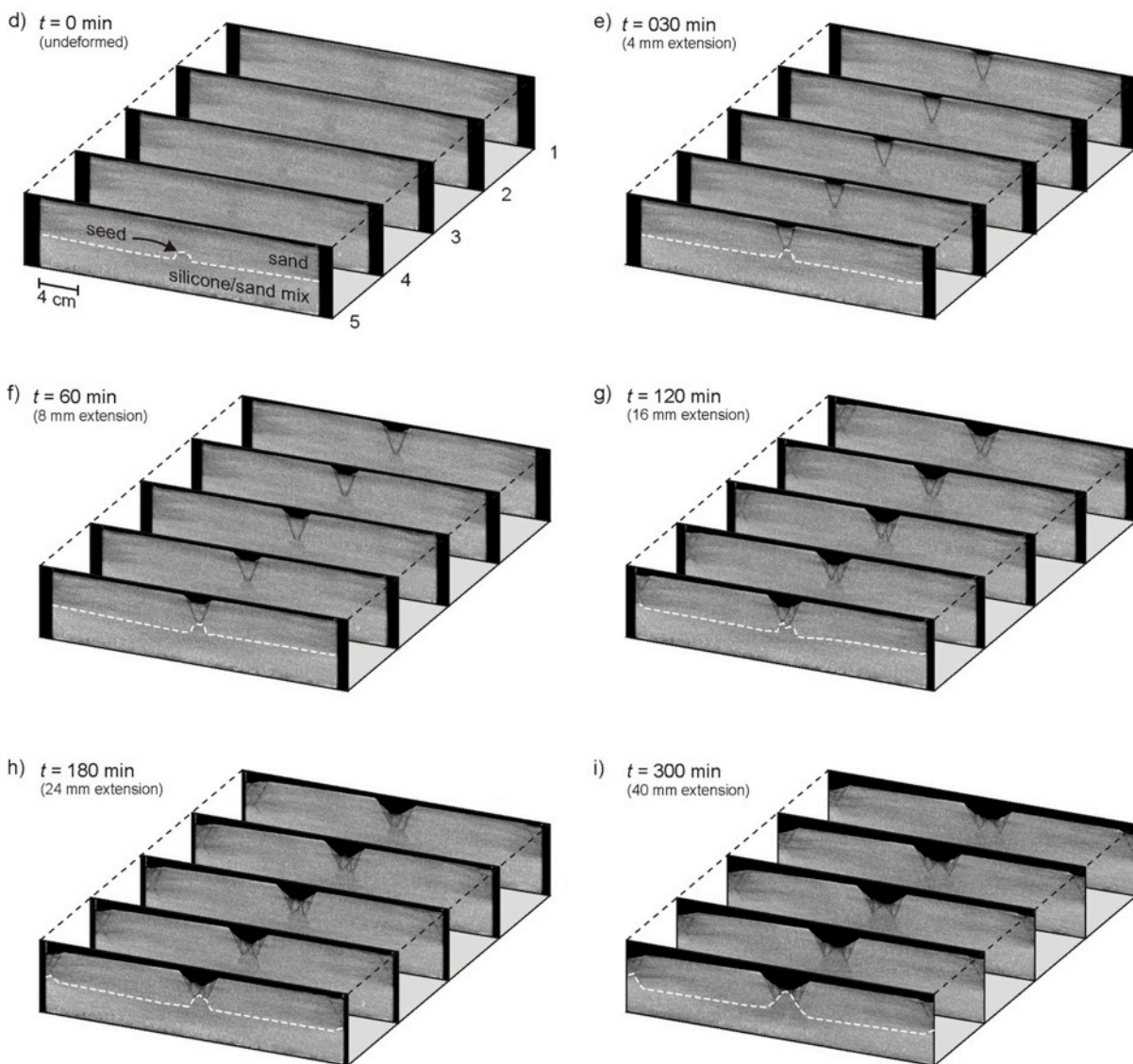
Fig. 6. Detailed DIC analysis of Models O1, O3, R1 and R3, depicting the top views shown in Fig. 5 and sequential cross-strike displacement (in y-direction, 30 minute increments) plotted along various along- and across strike profiles. Profile locations are shown on the top views and in Fig. 5. Thick dotted lines indicate seed traces. See (a) for scale. Black circles indicate the rotation axis in rotational extension models. a-s: across-strike.

1429  
 1430  
 1431  
 1432  
 1433  
 1434  
 1435  
 1436  
 1437  
 1438  
 1439  
 1440  
 1441

### Orthogonal extension model O3 - 3D CT images



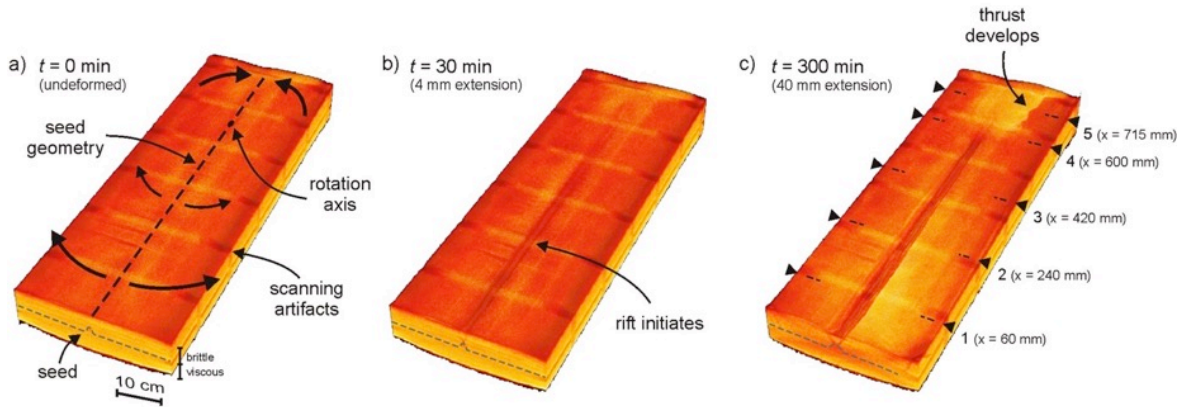
### Orthogonal extension model O3 - serial CT cross-sections



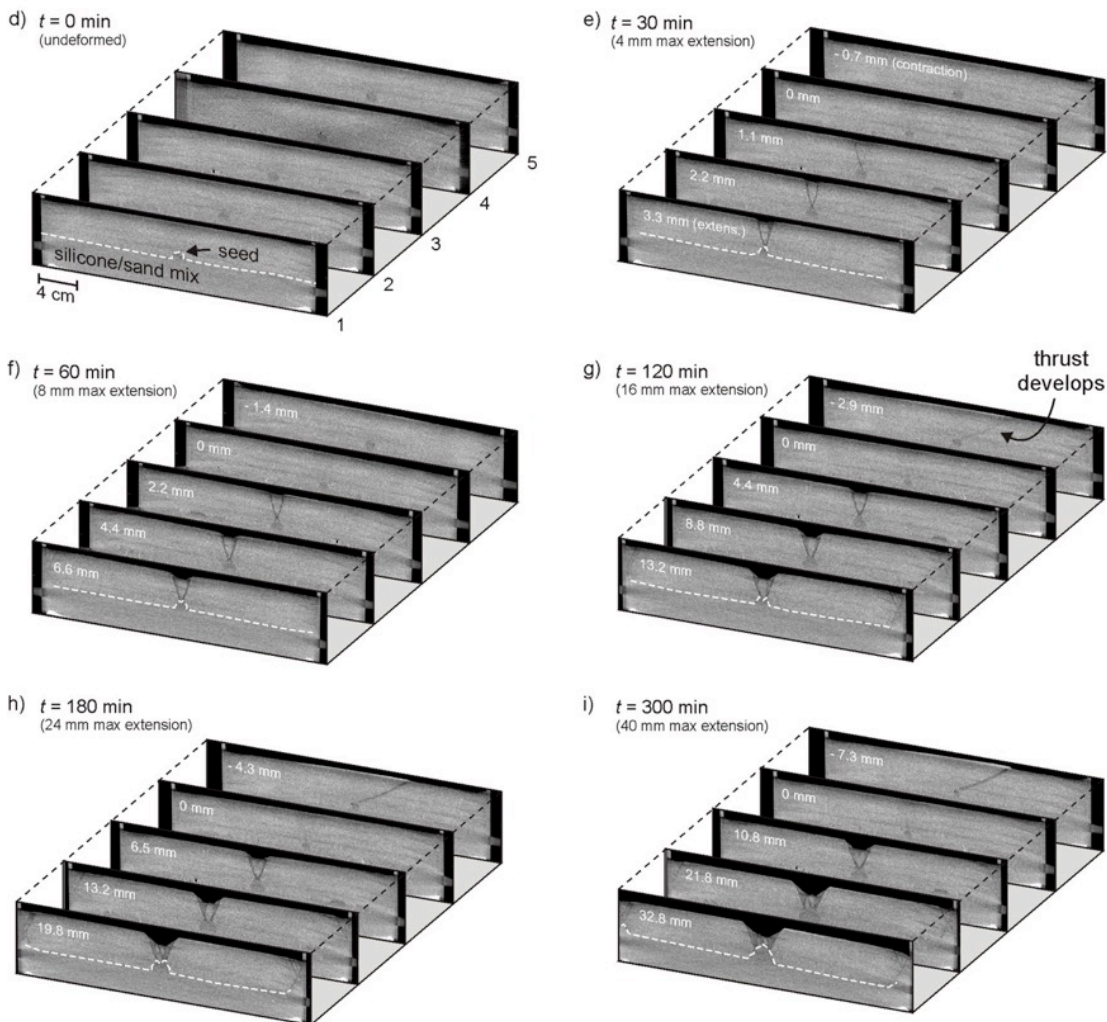
1442  
1443  
1444  
1445  
1446  
1447

Fig. 7. CT-derived 3D images (a-c) and serial cross-sections (d-i) depicting the external and internal evolution of Model O3. (d) shows the location and x-coordinates of the cross-sections. Note that the color palettes represent CT scan intensities, related to variations in material densities and do not indicate topography.

### Rotational extension model R3 - 3D CT data



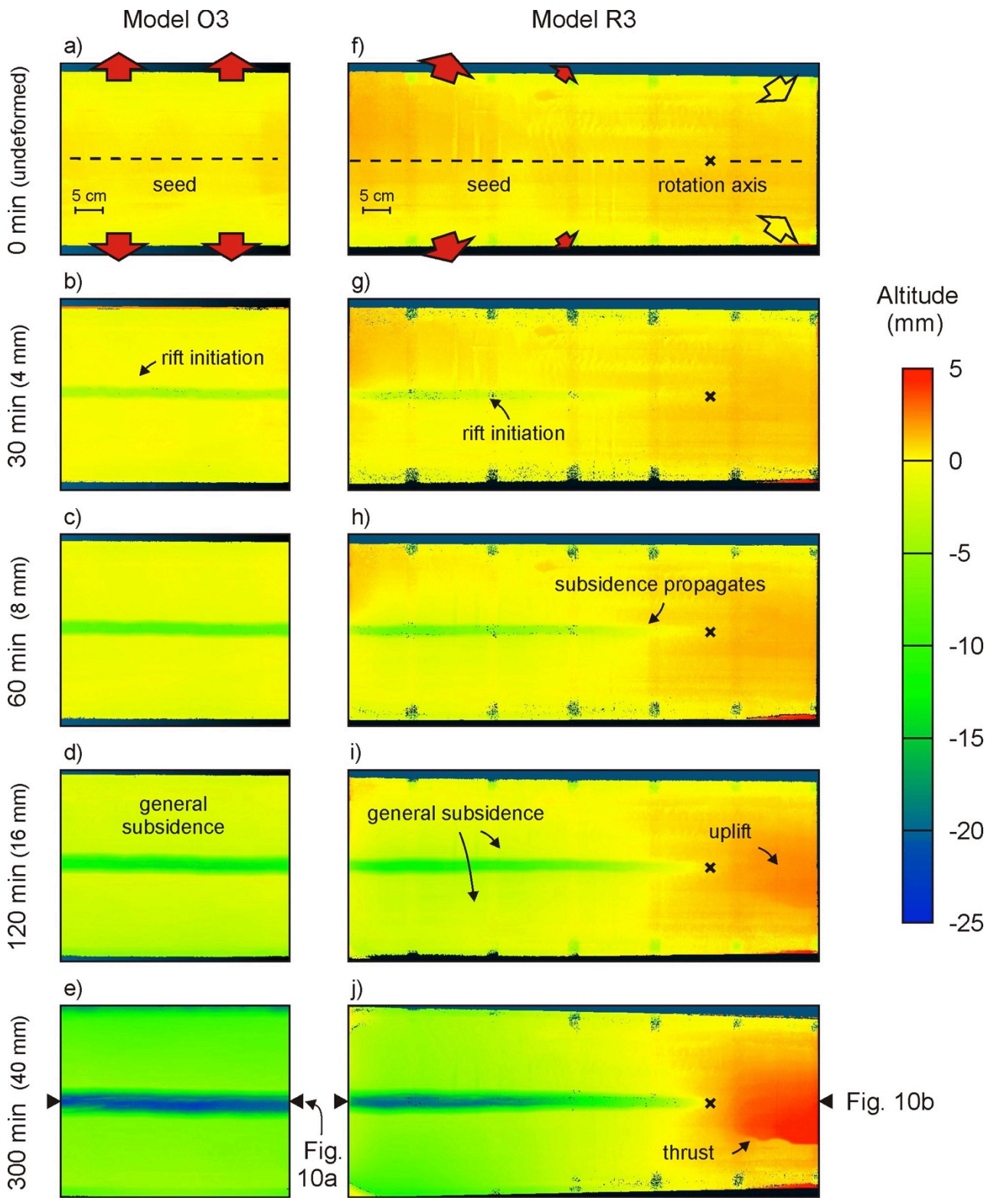
### Rotational extension model R3 - serial CT cross-sections



1448  
1449  
1450  
1451  
1452  
1453  
1454  
1455  
1456

Fig. 8. CT-derived 3D images (a-c) and serial cross-sections (d-i) depicting the external and internal evolution of Model R3. (c) shows the locations and x-coordinates of the cross-sections. (d-j). The applied extension is shown for every section, whereas the maximum extension values allow a direct comparison with model O3 (Fig. 7). Note that the color palettes represent CT scan intensities, related to variations in material density and do not indicate topography. The bright bands on the model surface images (a-c) are scanning artifacts, due to the design of the longitudinal sidewalls.

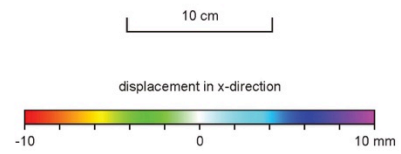
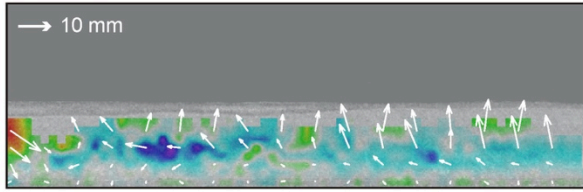
L457



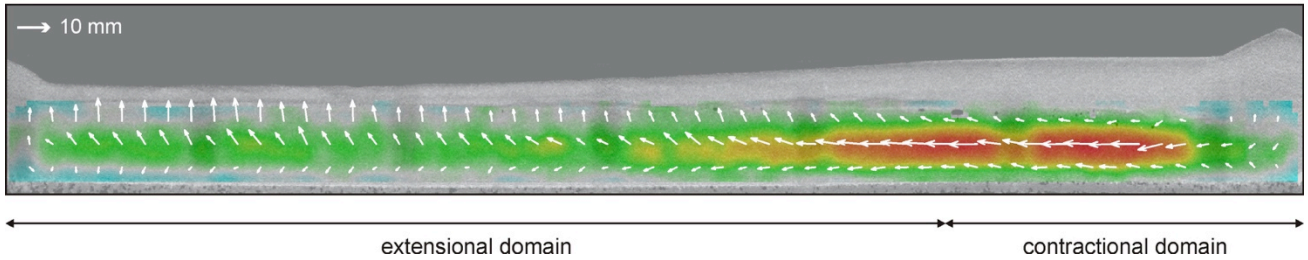
L458  
L459  
L460  
L461  
L462  
L463  
L464  
L465

Fig. 9. Topographic analysis of models O3 (orthogonal extension) and R3 (rotational extension) depicting the vertical displacements during model evolution. NB: The stripes in model R3 are scanning artifacts due to the design of the longitudinal sidewalls of the experimental apparatus and do not represent topographic variations. (Maximum) extension values are indicated to the left.

a) Model O3

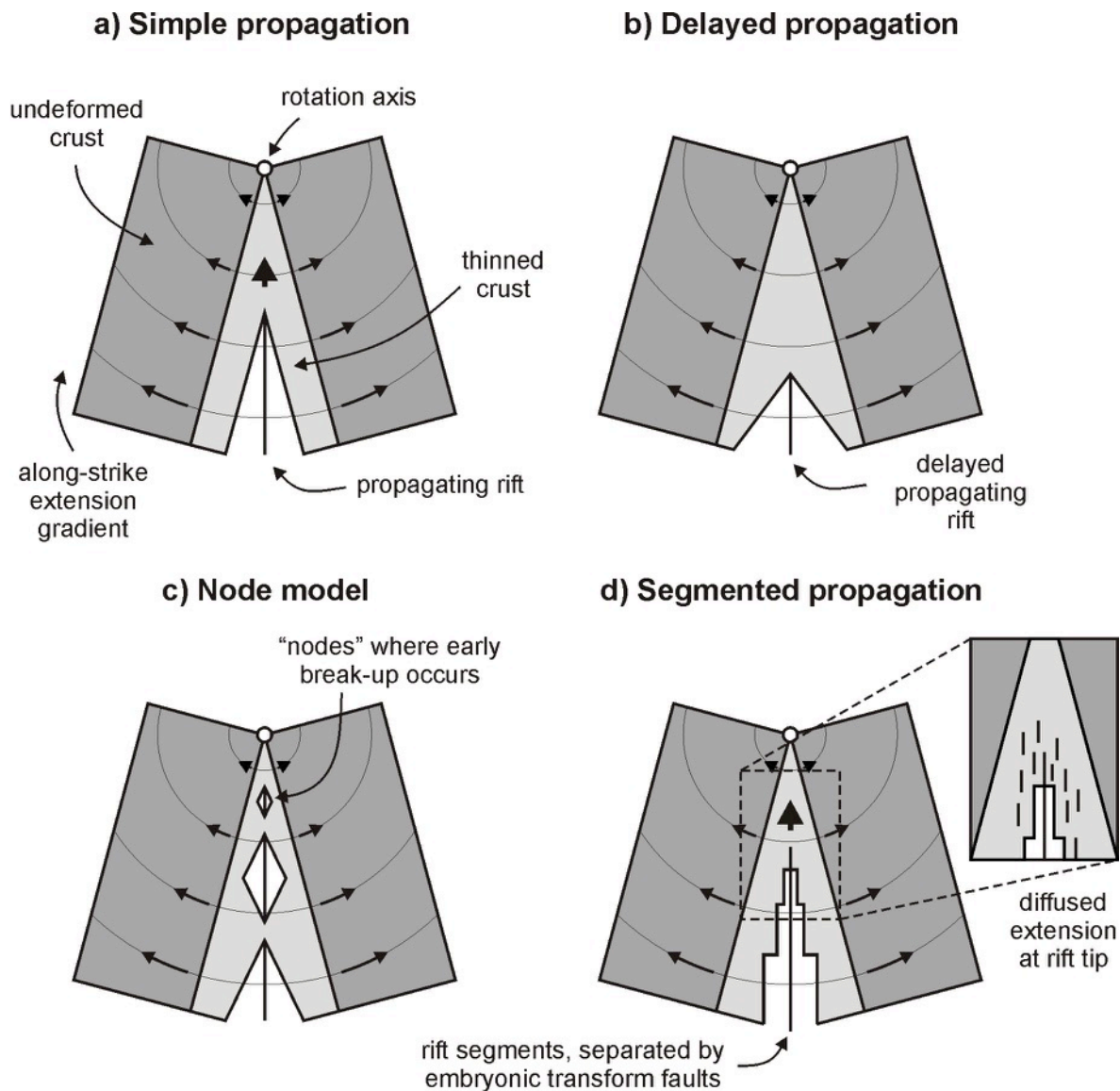


b) Model R3



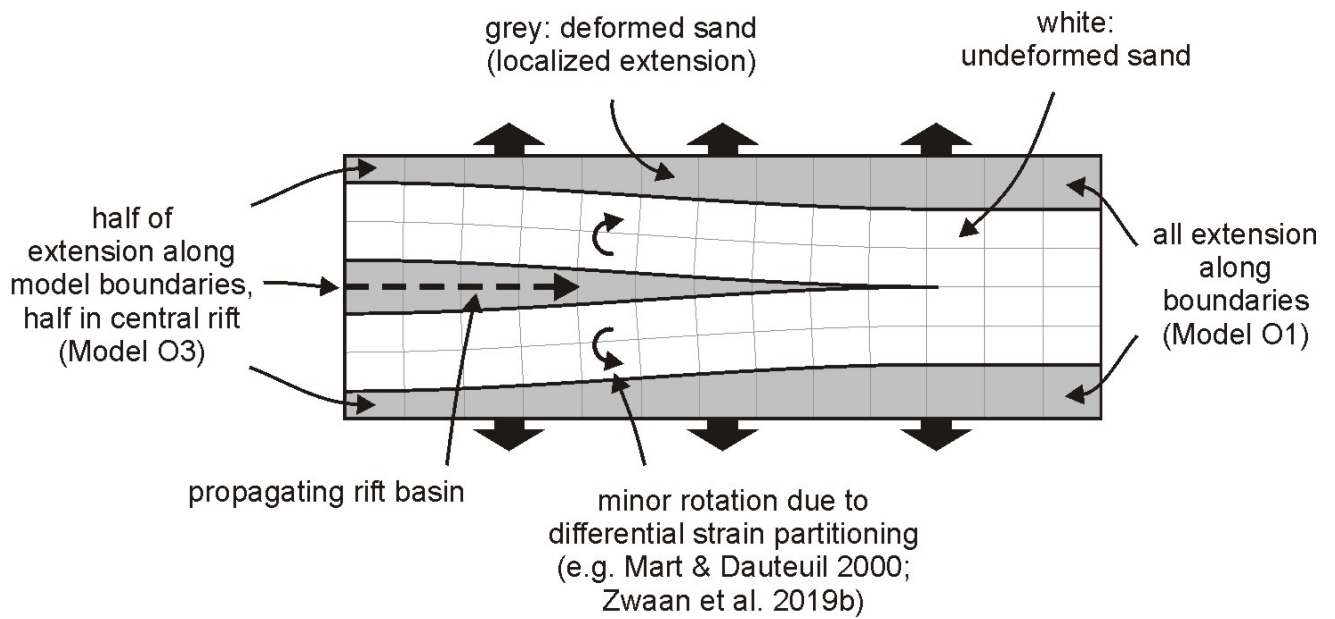
L466  
L467  
L468  
L469  
L470  
L471  
L472  
L473

Fig. 10. DIC analysis of along-strike CT sections from (a) Model O3 and (b) Model R3, revealing a significant flow of viscous material from the contractional domain to the extensional domain in model R3, whereas no clear along-axis motion is recorded in Model O3. Note that these results do not represent the full 3D flow field (see also the supplementary data in Zwaan et al. 2020). For section locations see Fig. 9.



1474  
1475  
1476  
1477  
1478  
1479  
1480  
1481  
1482  
1483  
1484  
1485  
1486  
1487  
1488  
1489

Fig. 11. Different models of rift propagation and break-up for rotational tectonic settings, compare with Fig. 1. (a) Simple propagation as seen in our models and proposed for the Red Sea and other ultra-slow spreading ridges (Augustin et al. 2014). Modified after Martin (1984) and Augustin et al. (2014). (b) Alternative delayed break-up model inspired by Mondy et al. (2018). (c) Node model proposed for the Red Sea, in which break-up initiates simultaneously at various locations along the rift axis, due to asthenospheric influences (e.g. Souriot 1982; Figi et al. 2012, Fig. 2a, b). However Augustin et al. (2014) demonstrate that the apparent nodes on the sea floor are most likely due to basinward sediment flow that partially covers the rift axis. Still various analogue models develop node-like structure (e.g. Sun et al. 2009; Molnar et al. 2017, 2018). Image modified after Martin (1984) and Augustin et al. (2014). (d) Distributed rifting and segmented propagation as observed in the Woodlark Basin, Gulf of Aden and the Laptev Margin (Manighetti et al. 1997, Taylor et al. 1999; Franke & Hinz 2009, Fig. 2b, c, f).

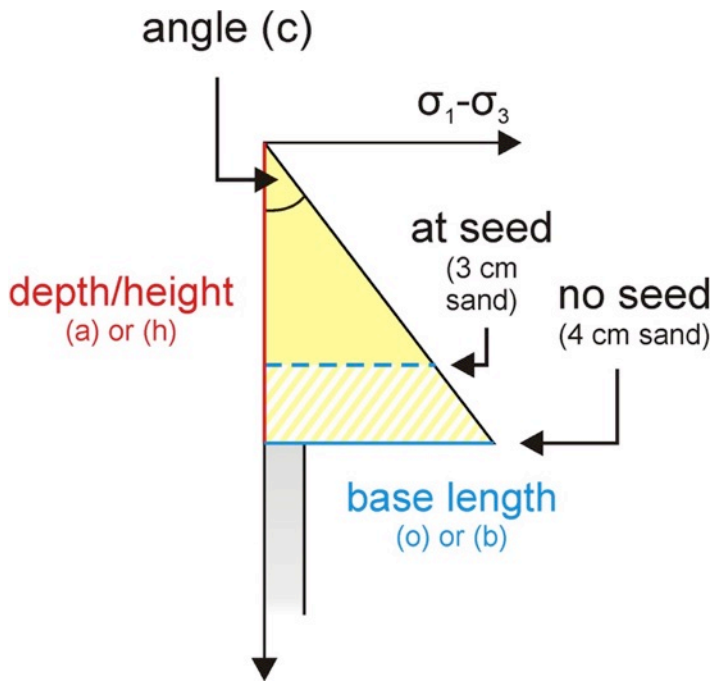


1490  
 1491  
 1492  
 1493  
 1494  
 1495  
 1496  
 1497  
 1498  
 1499  
 1500

Fig. 12. Effects of strain partitioning in orthogonal extension models shown in map view, based on experimental results from this and previous studies. Left: situation observed in our model O3 (with seed) and strain partitioning between the model boundaries and a central rift. Right: situation observed in our model O1 with deformation exclusively concentrated along the model boundaries. Center: transition between two modes, involving local rotational extension and associated rift propagation due to differential strain partitioning as observed by Mart & Dauteuil (2000) and Zwaan et al. (2020).

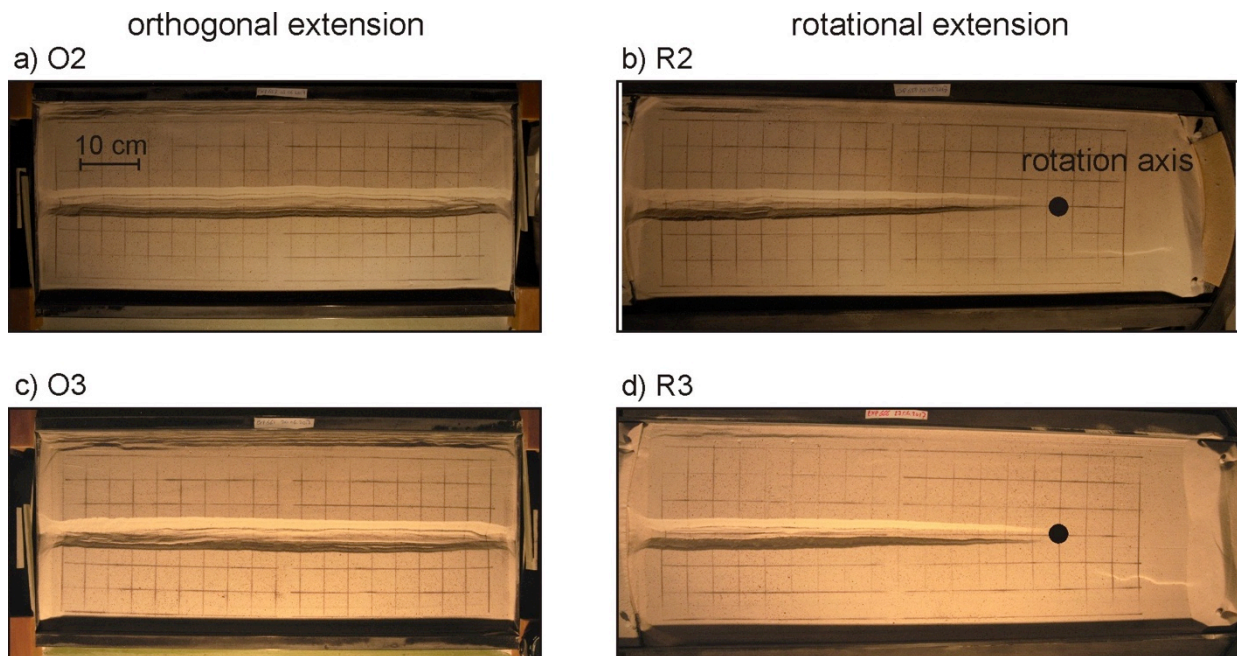
1501  
1502  
1503

### Appendix A



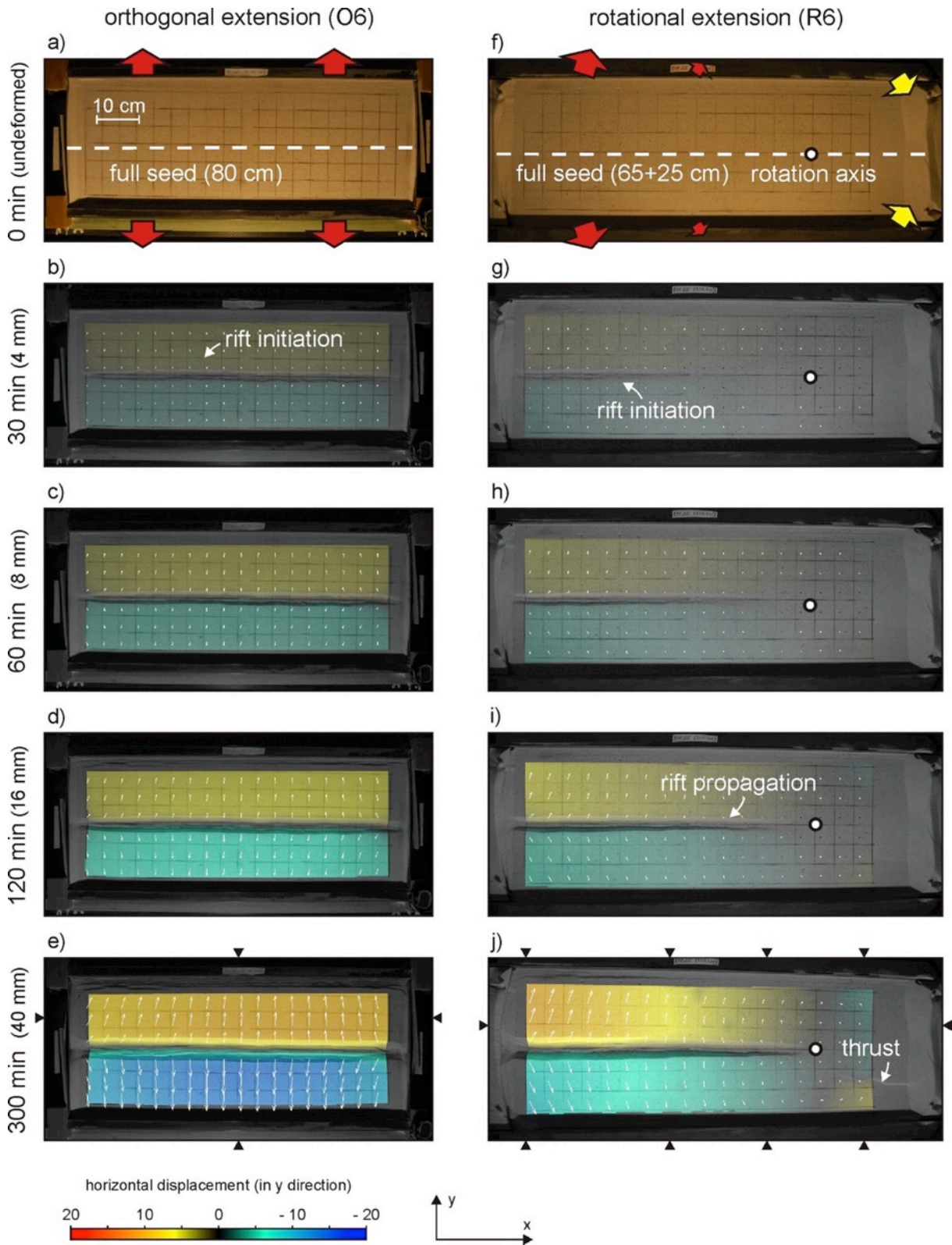
1504  
1505  
1506  
1507  
1508  
1509  
1510  
1511

Fig. A1. Definition of parameters used for brittle strength ratio calculations. Yellow indicates the sand layer, grey the underlying viscous layer. Compare to Fig 3e.



1512  
1513  
1514  
1515  
1516  
1517

Fig. B1. Surface view images of models O2 and R2 (with full seed) compared to their CT-scanned counterparts O3 and R3, illustrating the reproducibility of our model results.



1519  
 1520  
 1521  
 1522  
 1523  
 1524  
 1525

Fig. C1. Surface evolution and DIC map view results of models without seed: O3 (left) and R3 (right). White arrows indicate total cumulative horizontal displacement, whereas colors display across-strike (i.e. in y-direction). The triangles along the margins of the images indicate the locations of sections along which deformation is plotted in Fig. 6.